

1N-114  
067123

# InGaAsSb/GaSb Thermophotovoltaic Cells Phase I Effort

Yabo Li, Gary S. Tompa, Nancy Morris,  
John Connolly, and Hao Lee  
*Structured Materials Industries, Inc.*  
*Piscataway, New Jersey*

September 1997

Prepared for  
Lewis Research Center  
Under Contract NAS3-96060



National Aeronautics and  
Space Administration



---

---

# **InGaAsSb/GaSb Thermophotovoltaic Cells Phase I Effort**

## **Final Report**

**Prepared for  
Ballistic Missile Defense Organization**

**Contract Monitor:  
David Wilt  
NASA Lewis Research Center  
21000 Brookpark Rd.  
M.S. 302-1 Cleveland, Ohio 44135**

**Prepared by  
Structured Materials Industries, Inc.  
120 Centennial Ave.  
Piscataway, NJ 08854**

**and**

**David Sarnoff Research Center  
CN5300  
Princeton, NJ 08543-5300**

**February 21, 1997**

---

---



# Contents

<b>PROGRAM OBJECTIVES</b>	<b>2</b>
<b>SUMMARY</b>	<b>3</b>
<b>1.0 INTRODUCTION</b>	<b>4</b>
<b>2.0 DEVICE DESIGN</b>	<b>5</b>
<b>3.0 MATERIAL GROWTH/CHARACTERIZATION</b>	<b>9</b>
3.1 Material Growth	9
3.1 Material Composition	11
3.2 Material Doping	12
3.3 Carrier Mobility	13
3.4 Material Absorption	14
3.5 Surface Morphology	16
<b>4.0 TPV CELL GROWTH/FABRICATION</b>	<b>17</b>
4.1 TPV Structure	17
4.2 TPV Device Fabrication	17
<b>5.0 TPV CELL PERFORMANCE</b>	<b>20</b>
5.1 I-V Characterization	20
5.2 External Quantum Efficiency	25
<b>6.0 TPV MODELING</b>	<b>27</b>
6.1 Minority-Carrier Diffusion Model	28
6.2 Fit to Experimental Results	30
6.3 Optimized TPV Cell Design	35
<b>7.0 CONCLUSION</b>	<b>37</b>
<b>8.0 REFERENCES</b>	<b>40</b>

## **PROGRAM OBJECTIVES**

The goal of this phase I effort is to demonstrate the growth and fabrication techniques for an InGaAsSb-based thermophotovoltaic (TPV) cell operating out to 2.5  $\mu\text{m}$  that will enable efficient electrical power production from either exothermic reactions (fuel combustion) or radioisotope thermal sources. The TPV cells will be grown by molecular beam epitaxy (MBE) and consist of an InGaAsSb double-heterostructure fabricated on a GaSb substrate. The InGaAsSb composition will be lattice matched to the GaSb substrate to eliminate dislocations densities at the growth interface, a common problem with InGaAs-based TPV cell technologies. A p-on-n configuration will be used to reduce overall free carrier absorption for the incorporation of a back surface reflector.

## **SUMMARY**

Our Phase-I TPV development effort focused on the fundamental device issues such as material absorption and transport properties. This was deemed necessary since little or no InGaAsSb characteristic data are available. The material properties, such as carrier mobility and absorption, that were determined during this program are very important for determining the structure parameters for optimized TPV devices. Using this technical approach, we are now able to predict the spectral response of proposed TPV structures by inputting known material properties into a computer modeling program developed at Sarnoff. This computer aided design modeling will accelerate the development cycle of InGaAsSb-based TPV cells and reduce the technical risk of future development efforts.

The major achievements completed in this phase I effort are:

- Critical design issues relating to carrier transport investigated.
- InGaAsSb characteristics important to TPV cell design determined.
- Growth parameters and fabrication processes for InGaAsSb TPV cells determined.
- Prototype InGaAsSb TPV cells grown and evaluated.
- Computer modeling program developed to predict spectral quantum efficiency.
- Carrier diffusion lengths and surface/interfacial recombination velocities determined.
- Dark-forward I-V characteristic identified as key to predict open circuit voltage.
- Superior spectral quantum efficiency for InGaAsSb TPV cells achieved.
- Optimized TPV structure design obtained by computer model.

## 1.0 INTRODUCTION

The focus of this Phase I effort has been modified slightly from the original scope. Early in the program it was decided that the fabrication and characterization of large area cells would be redirected to Phase II so that more emphasis could be placed on obtaining a fundamental understanding of the InGaAsSb TPV structures. This would give us a better footing for device optimization and scaling to larger area devices in Phase II.

In this Phase I effort we initially examined the general design issues (Section 2.0) associated with developing a 0.55 eV InGaAsSb-based TPV cell. Energy-band diagrams of TPV structures were constructed to understand the photo-excited carrier flow in the structure and to identify aspects of the structure which might possibly limit device performance.

The growth parameters for TPV layer antimonide-based compounds were determined and the material properties important to TPV cell performance, including material doping, carrier mobility, material absorption, and surface morphology, were determined (Section 3.0). Knowledge of these material properties are crucial to the design and modeling of the TPV structures.

Several p-on-n TPV structures were grown and processed into small-area (100- $\mu\text{m}$  diameter) etched-mesa devices to evaluate the performance characteristics (Section 4.0). The processing techniques for large-area (1  $\text{cm}^2$ ) cells having a metallized grid contact were also developed and demonstrated on a test TPV sample.

The dark I-V characteristics and the spectral quantum efficiency (SQE) of the TPV devices were evaluated (Section 5.0). The SQE data were fit to a one-dimensional model of photo-generated minority-carrier diffusion within the cell (Section 6.0) using the measured material and cell properties (i.e. carrier mobility, absorption constants and coating reflectivity). From the model fit the electron and hole diffusion lengths and the interfacial recombination velocities were obtained. Using these device parameters, the optimal p-on-n and n-on-p structures were calculated. Both of these theoretical device configurations had integrated quantum efficiencies of about 60%. Their relative integrated responses to a 1000  $^\circ\text{C}$  blackbody were both about 50%.

Methods to improve TPV cell performance are discussed in Section 7.0 and will be examined in further detail in the Phase II proposal.



## 2.0 DEVICE DESIGN

The design issues associated with developing a 0.55 eV InGaAsSb-based TPV cell have been examined. A schematic diagram of the structure considered in this examination is shown in Figure 1. The device comprises a 0.55-eV bandgap InGaAsSb photocell

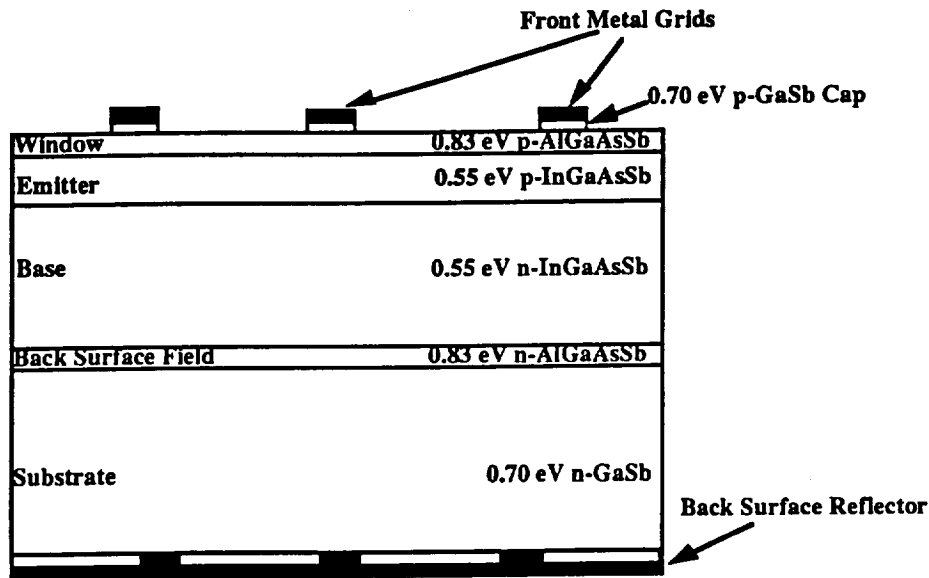


Figure 1. Schematic diagram of the 0.55 eV InGaAsSb TPV cell.

sandwiched between a 0.83 eV bandgap AlGaAsSb back-surface-field layer and a 0.83 eV bandgap AlGaAsSb window layer all grown on an n-GaSb substrate. The back-surface-field layer reflects photo-generated holes toward the p-n junction. The window layer transmits radiation above 1.5  $\mu\text{m}$  wavelengths, physically protects the p-InGaAsSb emitter, and also reflects photo-generated electrons toward the p-n junction. A p<sup>+</sup> GaSb cap layer beneath the metal grid improves Ohmic contact. A back-surface-reflector is incorporated to recuperate photons with energies less than 0.55 eV.

Energy-band diagrams of the TPV structure were constructed to understand the photo-excited carrier flow in the structure and to identify aspects of the structure which might possibly limit device performance. Figure 2 shows a schematic diagram of the equilibrium energy bands for the p-on-n device. The conduction and valence bands,  $E_c$  and  $E_v$ , are

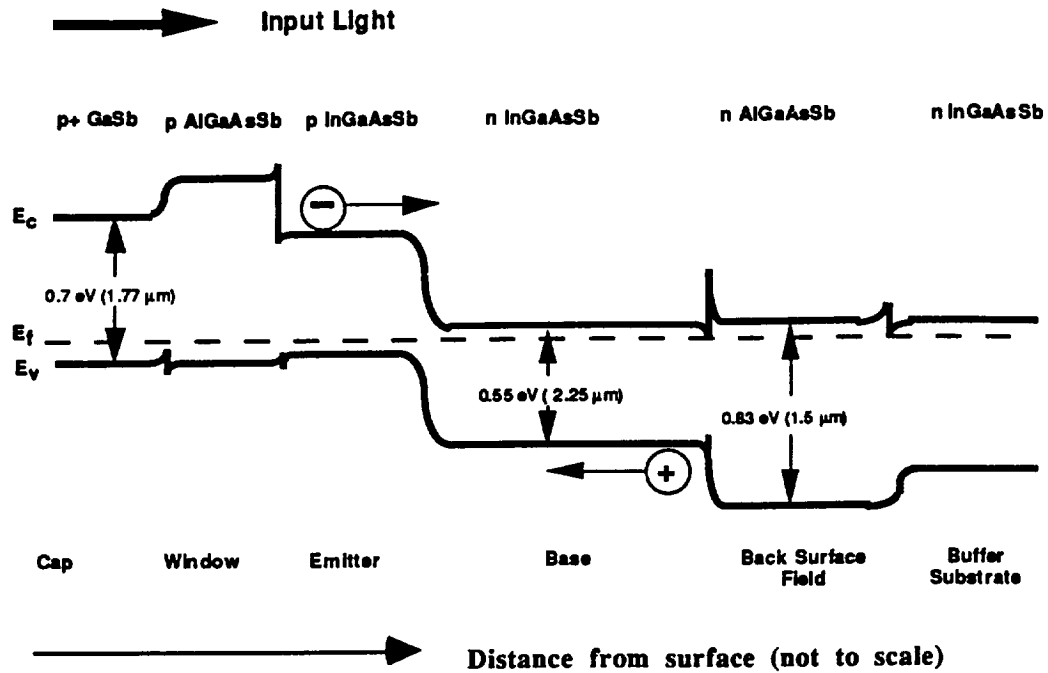


Figure 2. Schematic energy-band diagram of an 0.55 eV InGaAsSb p-on-n TPV device

shown, along with the Fermi level. Radiation enters from the left and is absorbed in the emitter and the base. The n-GaSb substrate is at the right. The general flow of photoexcited electrons and holes is indicated. The bandgaps of the layers are to scale, but the layer thicknesses are not. The band offsets at the heterojunctions are calculated from the data of Tsou [1], which in Sarnoff's experience gives the closest agreement with experiment.

Radiation energy below 0.7 eV is transmitted through the GaSb cap and the AlGaAsSb window layers. Radiation energy between 0.7 eV and 0.55 eV is predominately absorbed in the InGaAsSb emitter and base regions of the device; photoexcited electrons drift and diffuse toward the n-contact, whereas holes move toward the p-contact. To absorb 0.55 eV radiation requires that the InGaAsSb have an In-content of 19%. The window layer provides a reflecting barrier for electrons, and the back-surface-field layer provides a reflecting barrier for holes, as shown in Fig. 2. Without these barriers, the current would be reduced to about one half its value.

### Limitations to efficient carrier transport

Electrons swept into the base from the emitter encounter an abrupt electron barrier at the base/back-surface-field interface. In operation this heterojunction is a reverse-biased

Schottky junction with a barrier height of 0.32 eV ( $> 10$  kT at room temperature). This can be a major problem, since tunneling through the 0.32-eV barrier requires a bias voltage. This effect will reduce the output power, and hence, the efficiency, of the device. Also, electrons trapped at this interface in the base can readily recombine with holes photo-generated there, again leading to a loss in device efficiency. Grading the composition from InGaAsSb to AlGaAsSb at the base/back-surface-field interface while maintaining the lattice match, will greatly reduce the voltage drop across the heterojunction. Sarnoff has demonstrated the effectiveness of using a compositionally-graded interface for very low voltage heterojunctions in antimonide-based lasers [2].

As discussed above, the window layer presents a reflecting barrier to electrons photo-generated in the emitter. Depending on the p-doping levels of the emitter and window layers, there may be a slight downward bending of the bands in the emitter at the heterojunction. This notch in the conduction band attracts electrons, and if deep enough, it will act as a trap and may be a site of strong electron-hole recombination that would cancel the beneficial effects of the reflecting barrier. P-doping the window layer more heavily than the emitter causes the bands to bend upward in the emitter, eliminating the worrisome notch.

The notch in the emitter layer at the emitter-window interface can also be eliminated by grading the composition from InGaAsSb to AlGaAsSb at the interface while maintaining the lattice match. Maintaining the lattice match of this interface is critical since the quality of the heterojunction strongly affects the recombination velocity of electrons striking the barrier [3].

During operation, the cap/window heterojunction is biased like a forward-biased Schottky barrier with holes flowing from the AlGaAsSb window layer into the cap. Thus, there will be a small voltage drop across the heterojunction that reduces the efficiency of the device. Again, grading the composition from AlGaAsSb to GaSb, while, of course, maintaining the lattice match, will greatly reduce the voltage drop across the heterojunction. In addition, a heavily p-doped cap and window can also be utilized to reduce the voltage drop across this heterojunction. Heavily p-doping the AlGaAsSb layer will thin the barrier; since the effective width of the barrier scales inversely with the square root of the doping concentration, the valence band will bend more sharply.

The remedies, discussed above, for increased carrier transport efficiency through composition and doping tailoring will not be pursued during this Phase I effort but could be investigated during Phase II on more advanced structures.

### **General Design Considerations**

One of the most important properties of any photodiode is the dark current density,  $J_D$ .  $J_D$  determines the open-circuit,  $V_{OC}$ , through the well-known formula

$$V_{OC} = nkT \ln(J_{SC} / J_D)$$

$n$  is the ideality factor for  $J_D$  in the InGaAsSb, emitter-base p-n junction,  $k$  is Boltzmann's constant,  $T$  is the temperature, and  $J_{SC}$  is the short-circuit photo-current.

At low currents  $n \approx 2$ , owing to recombination through mid-bandgap states in the depletion region. At higher currents  $n = 1$ , signifying minority-carrier injection under forward bias. The crossover voltage for these two branches depends on the particular characteristics of the p-n junction. We will measure the dark current of the emitter-base p-n junction, fitting it to the simple exponential dependence of diode current on diode voltage. In this way we can extract some of the parameters describing the dark current, such as the crossover voltage for the two branches. These empirical studies will also allow us to see the effects of different growth conditions on  $J_D$ .

In general,  $J_D$  is kept small by having high-purity emitter and base material, free of deep-level impurities that act as recombination centers and that increase  $J_D$ . We will monitor the InGaAsSb p-n junction dark current, comparing it with the theoretical values. We will adjust growth conditions to minimize the " $n = 2$ " branch of  $J_D$ .

Moderately high doping levels in the base and emitter minimizes the " $n = 1$ " branch of  $J_D$ , which is proportional to the minority-carrier concentrations. This is somewhat difficult to do with narrow-bandgap materials, since their intrinsic carrier concentrations are relatively large. We will seek the doping levels and growth conditions that produce a minimum value for the " $n = 1$ " branch of  $J_D$ .

$V_{OC}$  also depends on  $J_{SC}$ .  $J_{SC}$  is optimized in several ways. The largest possible fraction of the radiation between 1.5 and 2.25  $\mu\text{m}$  should be absorbed in the emitter and base. The

photogenerated carriers must efficiently diffuse to the p-n junction, which means that their diffusion lengths should be much longer than the widths of the base or emitter. Architectures employing a BSR reflect a large portion of the non-absorbed radiation, so there is a second pass of this light back through the emitter and the base, which effectively increases their widths. This effect increases  $J_{SC}$  by enhancing photon absorption.

Optimization of  $V_{OC}$  and  $J_{SC}$  is a major task in developing efficient 0.55-eV TPV cells. This optimization will be accomplished by adjusting the target TPV cell parameters (layer thickness and doping level) and the growth conditions based on material and TPV cell characterization.

### 3.0 MATERIAL GROWTH/CHARACTERIZATION

#### 3.1 Material Growth

All of the TPV structures for this program were grown in a dual-chamber Intervac (formerly Varian) molecular beam epitaxy/metalorganic molecular beam epitaxy (MBE/MOMBE) system. This state-of-the-art system, shown in Fig. 3, features

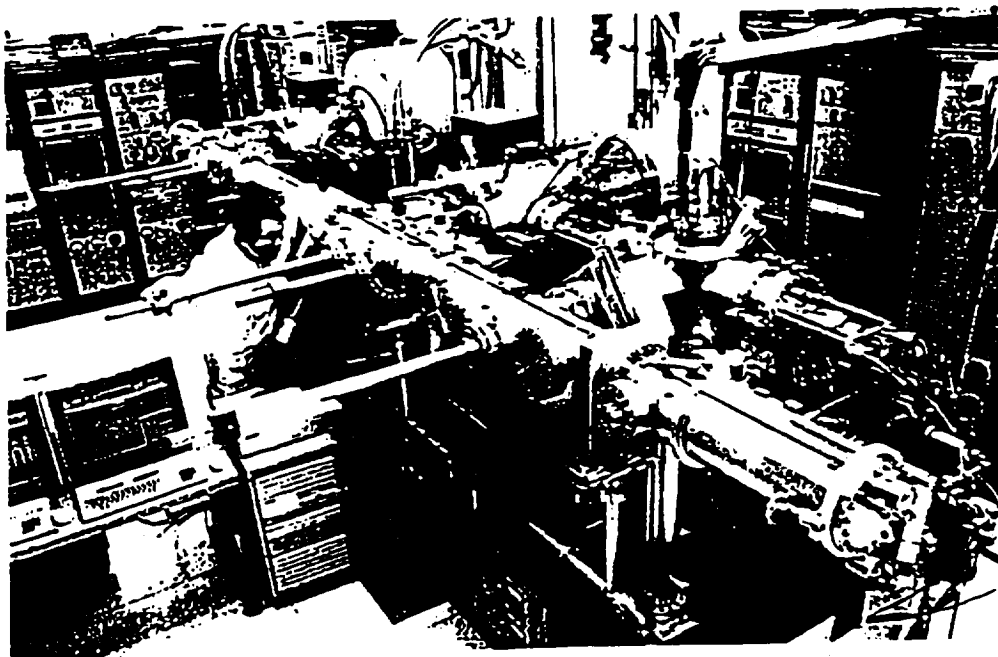


*Figure 3.* MBE/MOMBE growth system.

submonolayer thickness control, excellent uniformity over 3-in. wafers, and *in-situ* transferability between the MBE and MOMBE growth chambers for the optimization of material structures. The TPV structures were grown in their entirety in the MBE chamber of the system.

### General Growth Issues

There are two major issues in the MBE growth of Sb-based alloys for TPV cells. First, accurate compositional control is essential to obtain uniform layers having the desired bandgap and lattice constant. Lattice-mismatched compositions generate dislocation defects resulting in high dark currents and decreased TPV cell efficiency. Second, it must be possible to dope the materials both n- and p-type. Since the doping density of the TPV layers must be optimized to obtain increased minority carrier lifetime in conjunction with low series resistance, accurate control of the doping levels is critical. In addition, movement of the p-n junction, caused by dopant diffusion, is also a concern for structures containing high doping levels.

The Sb-based quaternary compounds required in the TPV structures were grown using the sources listed in Table 1. The flux control of the group-V beams, is relatively difficult, due to the high and different vapor pressures in group-V solid sources, resulting in an imprecise fraction of group-V constituents in semiconductors like AlGaAsSb and InGaAsSb. To facilitate the accurate control of As and Sb fractions in AlGaAsSb and InGaAsSb, an arsenic valved cracker has been successfully used to fine-tune the Group V flux ratios. Using the valved cracker, lattice-matched InGaAsSb and AlGaAsSb of various compositions are routinely obtained.

**TABLE 1.** Selection of MBE Source Materials and Cell Design for Optimized AlGaAsSb/InGaAsSb Growth

Source Material	Purity	Effusion Cell
Arsenic (As)	7N5	Valved Cracker
Antimony (Sb)	7N	Standard
Gallium (Ga)	8N	Standard
Aluminum (Al)	6N	Standard
Indium (In)	7N	Standard
Beryllium (Be)	6N	Standard
GaTe	6N	Standard

Beryllium and GaTe were used as the p- and n-type dopants, respectively. GaTe is used instead of elemental Te since the high vapor pressure of the latter causes considerable concern about memory effects and complicated reactions with Ga to form  $\text{Ga}_2\text{Te}$  or  $\text{Ga}_2\text{Te}_3$ .

## Material Property Determination

### 3.2 Material Composition

The material compositions were determined on test layers grown on GaSb substrates, through a combination of x-ray diffraction, electron microprobe, and photoluminescence (PL). Figure 4 shows a photoluminescence plot for an undoped InGaAsSb lattice-matched to a GaSb substrate. The peak emission wavelength for this sample is approximately  $2.25\ \mu\text{m}$  corresponding to a 0.55 eV bandgap energy. The chemical composition for which 0.55 eV InGaAsSb is lattice matched to GaSb, is  $\text{In}_{0.14}\text{Ga}_{0.86}\text{As}_{0.12}\text{Sb}_{0.88}$ .

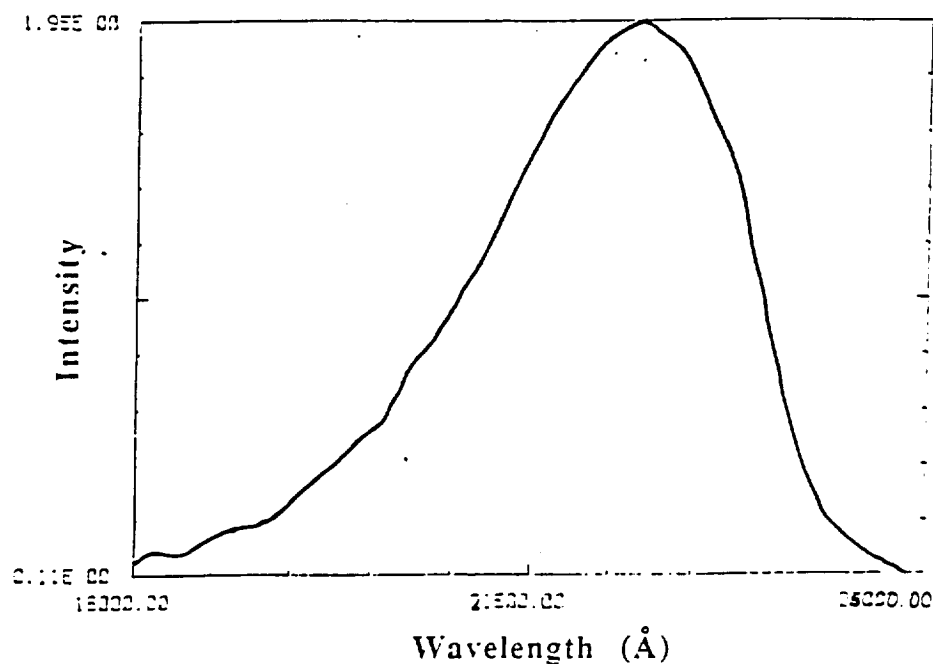


**Figure 4.** Photoluminescence plot showing emission intensity of 0.55 eV InGaAsSb as a function of wavelength.

### 3.3 Material Doping

Since insulating GaSb substrates are unavailable, the p and n-doping calibration have been achieved using Hall measurements of test layers grown on semi-insulating GaAs substrates. Figure 5 shows the carrier concentration for p-doped 0.55 eV InGaAsSb as a function of source temperature. Controlled p-doping of the InGaAsSb material up to a concentration of  $2 \times 10^{19} \text{ cm}^{-3}$  has been obtained. Similar p-doping behavior has been observed for both GaSb and AlGaAsSb materials.

Figure 6 shows the carrier concentration for both n-doped 0.55 eV InGaAsSb as a function

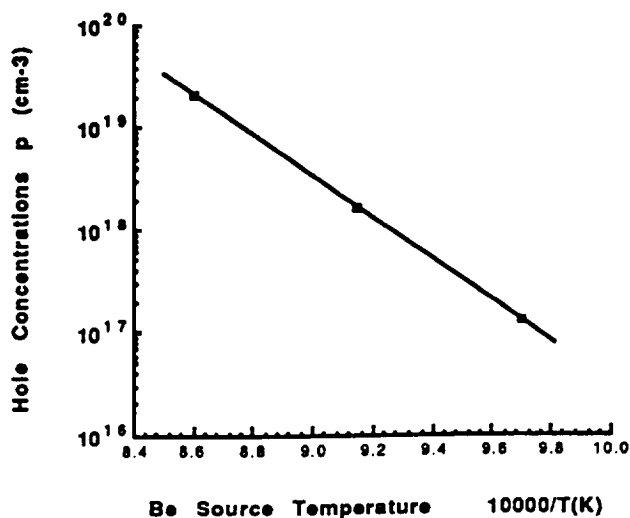


Figure 5. Hole concentration in 0.55 eV InGaAsSb as a function of Be source temperature.

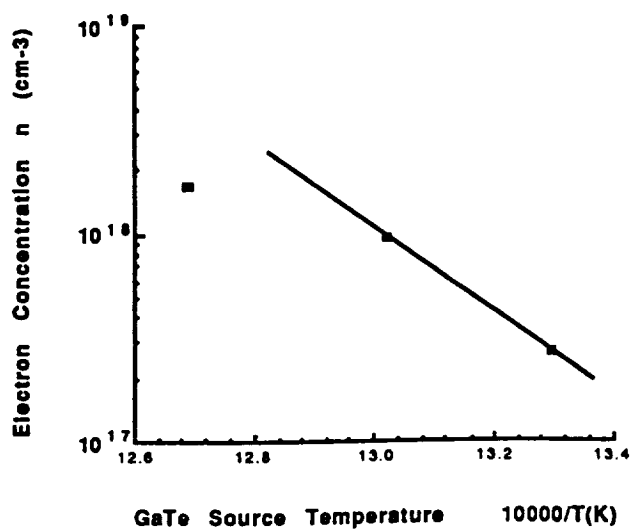


Figure 6. Electron concentration in 0.55 eV InGaAsSb as a function of GaTe source temperature.



of source temperature. As expected the carrier concentration begins to drop off above  $1 \times 10^{18} \text{ cm}^{-3}$ . Similar saturation levels ( $\sim 1 \times 10^{18} \text{ cm}^{-3}$ ) for n-doped GaSb have been observed by in our previous work and by other researchers [4].

### 3.4 Material Mobility

Figure 6 shows the mobility of electrons measured at 300 K for the 0.55 eV n-doped InGaAsSb test layers. For comparison, electron mobilities of n-GaSb test layers (doped with Te from a GaTe source) grown in our previous work and results from MIT-Lincoln Labs [5] are also included. For the n-doped GaSb the dependency of mobility to electron concentration can be explained as follows. For samples with the carrier concentration,  $n = (N_D - N_A)$ , less than the background acceptor concentration,  $N_A \sim 10^{16} \text{ cm}^{-3}$ , the mobility increases with  $n$  due to an increase in the electrostatic screening of the charged scattering centers. For samples with  $n$  greater than  $N_A$ , the mobility decreases as  $n$  increases due to an increase in the concentration of scattering centers ( $N_D + N_A$ ). This mechanism overcomes the effect of increased screening. The observed decrease in mobility for the 0.55 eV InGaAsSb material compared with the GaSb of equivalent carrier concentration is believed to be the result of alloy scattering in the quaternary material.

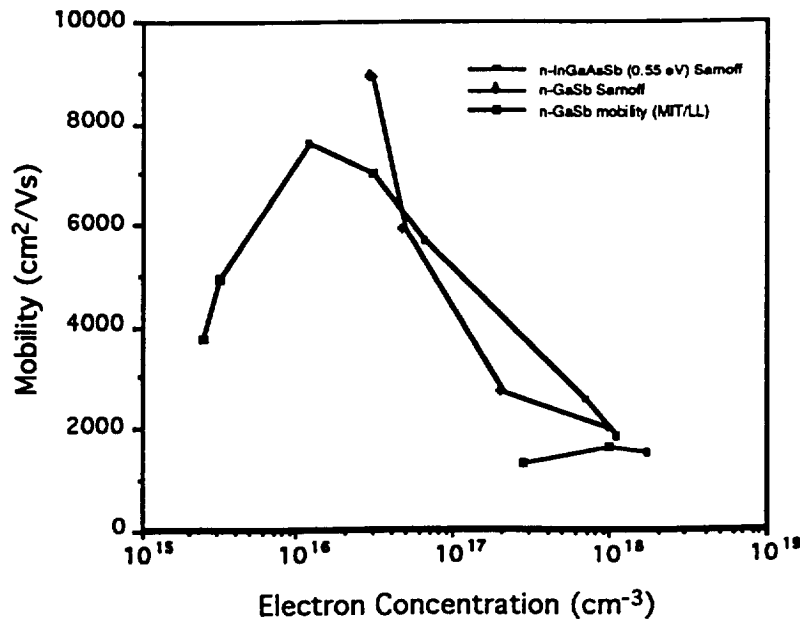


Figure 6. Electron mobility for 0.55 eV InGaAsSb and GaSb as a function of electron concentration.

Figure 7 gives mobility of holes measured at 300K for the 0.55 eV p-doped InGaAsSb test layers. For comparison, hole mobilities of p-doped GaSb test layers (doped with Be) grown in our previous work are also included. As in the n-doped InGaAsSb material, the observed decrease in mobility for the 0.55 eV InGaAsSb material compared with the GaSb of equivalent carrier concentration is believed to be the result of alloy scattering in the quaternary material.

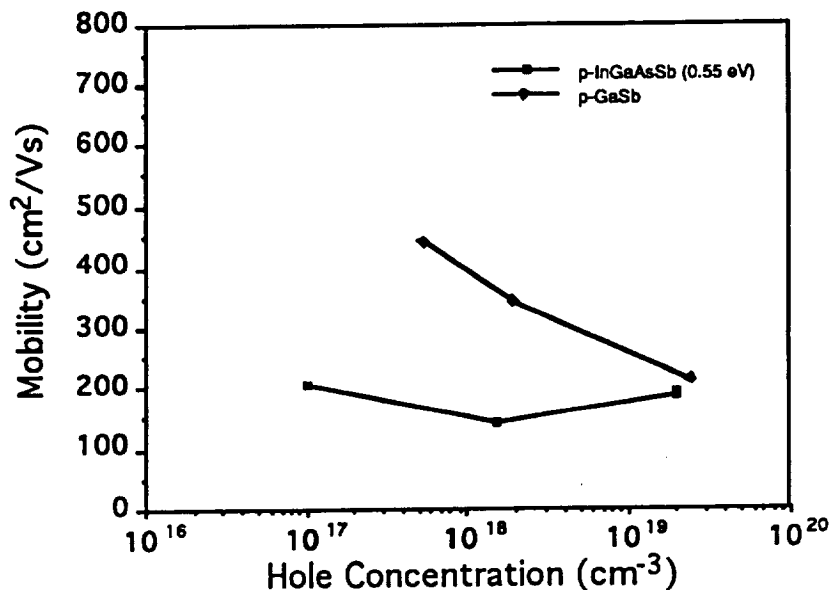
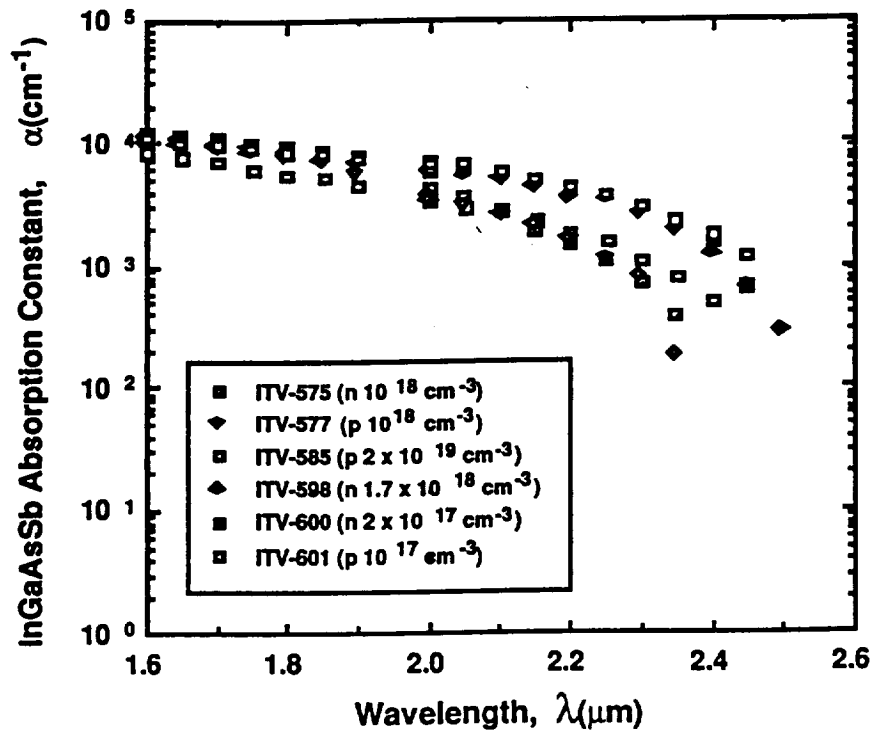


Figure 7. Hole mobility for 0.55 eV InGaAsSb and GaSb as a function of hole concentration.

### 3.5 Material Absorption

The absorption coefficient as a function of wavelength for n and p-doped 0.55 eV InGaAsSb layers grown on semi-insulating GaAs substrates is shown in figure 8. The absorption constant as a function of wavelength for a p-on-n TPV structure is shown in figure 9. The layer parameters of the TPV structure are shown in table 1. below. The absorption behavior of the single n- and p- doped InGaAsSb layers (discussed above) having similar doping levels as the TPV structure base and emitter layers, respectively, are also shown for comparison. The increase in absorption of the TPV structure for wavelengths below  $\sim 2.0 \mu\text{m}$  is due to absorption by the GaSb substrate.



**Figure 8.** Absorption constant as a function of wavelength for n- and p-doped InGaAsSb layers grown on semi-insulating GaAs substrates.

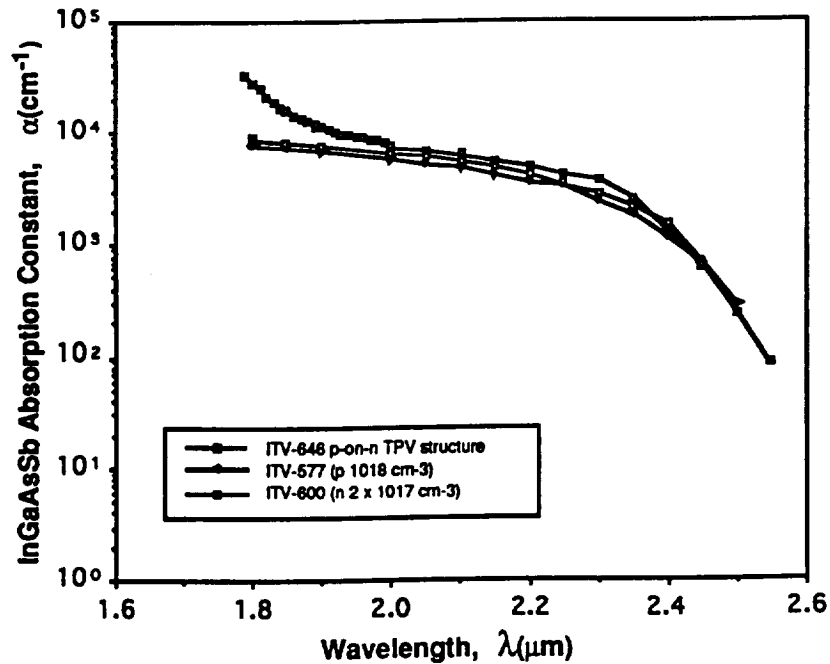


**Figure 9.** Absorption constant as a function of wavelength for n-on-p TPV structure and single n- and p-doped InGaAsSb layers (grown on semi-insulating GaAs substrates) having a similar doping level as the TPV structure base and emitter layers, respectively.

### **3.6 Surface Morphology**

Initial attempts to grow the TPV cells resulted in a very poor surface morphology which became worse with increasing layer thickness. In an attempt to eliminate the occurrence of defects observed for thick ( $> 1.0 \mu\text{m}$ ) InGaAsSb layers the indium effusion cell on the MBE reactor was replaced. Two potential problems were observed during the replacement of the cell: 1) a misalignment of the indium effusion cell shutter and 2) a discoloration of the indium source. We believe that the misalignment of the indium effusion cell shutter might be responsible for the metallic-looking defects. The shutter functions as an on/off switch to the indium flux. With the shutter in the closed (off) position, indium tends to deposit on the inner surface of the shutter. The alignment of the shutter prior to repair properly covered the cell in the off position but was partially open in the on position. We believe that the interaction of the indium-coated shutter with the indium flux while the shutter was in the on position might have contaminated the flux resulting in the observed defects. This is consistent with the sporadic rather than uniform density of defects observed.

The second observation, a discoloration of the indium source, is believed to be contamination of the indium with antimony. This is consistent with our observed decrease in actual indium incorporation (as determined by microprobe analysis) compared with calculated indium incorporation based on indium flux. Following replacement of the indium source the measured indium incorporation is consistent with calculated incorporation.

TPV cells grown for this program following the refurbishment of the MBE reactor have a significantly reduced density of metallic defects and a low to moderate density of oval defects. A reduction in the density of oval defects has been observed for recent InGaAsSb TPV structures grown in an on-going development program at Sarnoff following the growth of material (related to another Sarnoff program) requiring a large indium flux over an extended period of time. We suspect that the extended indium flux improved both the uniformity and quality of the newly charged indium source, which resulted in the improved surface morphology.

We have also observed that the majority of the oval defects are larger for structures having increased layer thickness, suggesting that the defects are formed in the early stages of

growth. One possible source is that the initial burst of indium flux might be contaminated by indium droplets as the shutter is opened. We are currently investigating modifying the indium shutter (possibly a reduced opening speed) to remedy this problem. The low density of square defects is a possible concern for large area cells and is being addressed in on-going other TPV cell development programs at Sarnoff.

## 4.0 TPV CELL GROWTH/FABRICATION

### 4.1 TPV Structure

Several p-on-n TPV structures were grown and processed into small-area (100- $\mu\text{m}$  diameter) etched-mesa devices to evaluate the performance characteristics. The layer parameters for a typical p-on-n TPV structure (ITV-646) are shown in Table 2.

*Table 2.* Parameters for the 0.55 eV InGaAsSb TPV cell.

Layer	Composition	Thickness (target)	Carrier Conc. (target)
Cap	p-GaSb	0.05 $\mu\text{m}$	$2 \times 10^{19} \text{ cm}^{-3}$
Emitter	p-In <sub>0.14</sub> Ga <sub>0.86</sub> As <sub>0.12</sub> Sb <sub>0.88</sub>	1.0 $\mu\text{m}$	$1 \times 10^{18} \text{ cm}^{-3}$
Base	n-In <sub>0.14</sub> Ga <sub>0.86</sub> As <sub>0.12</sub> Sb <sub>0.88</sub>	1.0 $\mu\text{m}$	$1 \times 10^{17} \text{ cm}^{-3}$
Buffer	n-GaSb	0.5 $\mu\text{m}$	$1 \times 10^{18} \text{ cm}^{-3}$
Substrate	n-GaSb	100-200 $\mu\text{m}$	$1-10 \times 10^{17} \text{ cm}^{-3}$

### 4.2 TPV Device Fabrication

#### Large Area TPV Cell Development

A portion of the ITV-646 TPV wafer was fabricated into a large area (1  $\text{cm}^2$ ) cell. (Although the surface morphology of this wafer was too poor to obtain characterization data for such a large area cell, fabrication techniques applicable to future TPV wafers runs were developed.) The front grid contact consisted of a central 0.5 mm wide bus bar having 10  $\mu\text{m}$  wide grid lines spaced 100  $\mu\text{m}$  apart. A "lift-off" masking technique was utilized to pattern the Ti-Pt-Au metallized grid. Standard Au-plating techniques could be used to achieve the required Au-film thickness. Figure 10 shows a portion of the front grid contact at a magnification of  $\sim 65\times$ .

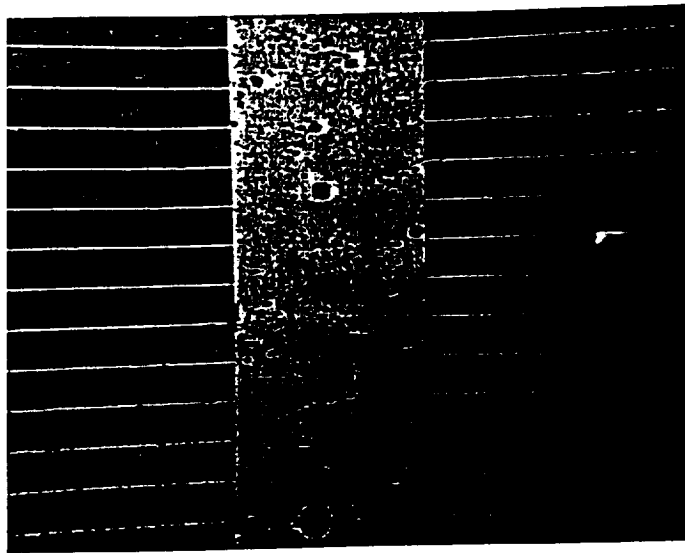


Figure 10. Front grid contact of 1 cm<sup>2</sup> TPV wafer (ITV-646).

The back-surface of the wafer was mechanically thinned to a thickness of 7 mils and chemically polished using a bromine-methanol solution. AuGeNiAu, alloyed using a rapid thermal anneal process, was used for the back contact.

### Small-area (100 $\mu\text{m}$ -diameter) Mesa Devices

Figure 11 shows a schematic diagram of the mesa (snowman) device configuration that

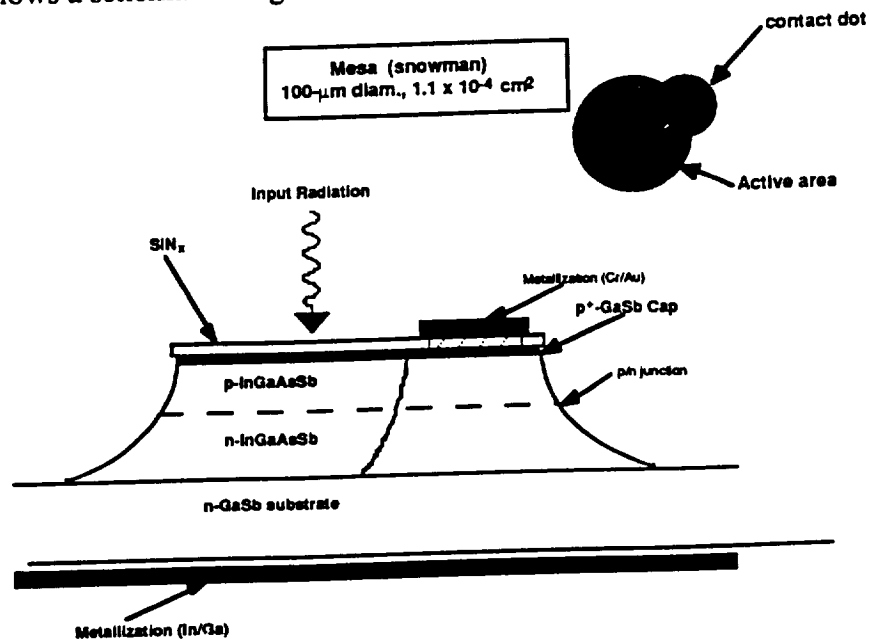
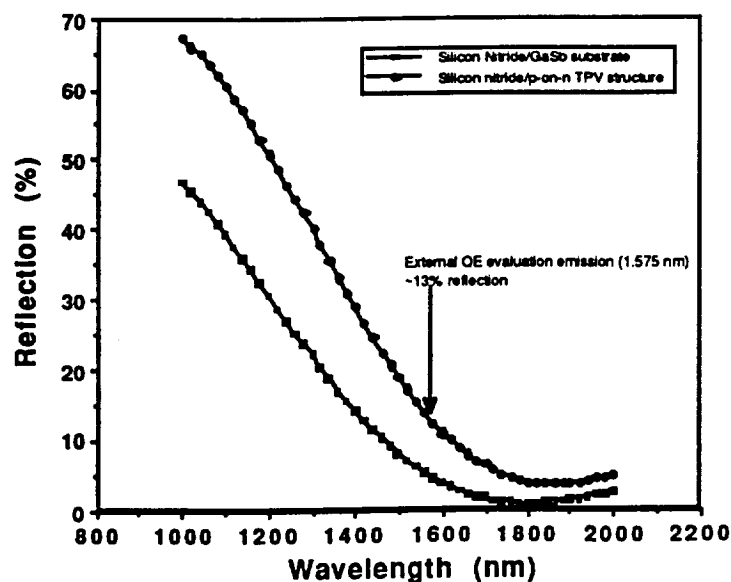


Figure 11. Small-area (100  $\mu\text{m}$  diameter) mesa test structure.

was used to evaluate the performance characteristics of the TPV structures. The mesa region contains a 100  $\mu\text{m}$ -diameter active area and a 50  $\mu\text{m}$ -diameter contact dot and is formed using a bromine-methanol chemical etch. The front and rear contact metallizations are Cr/Au and Sn/Ni/Au, respectively. Initial attempts to form the front contact dot resulted in poor adhesion between the GaSb cap and Cr interface leading to a large series resistance as discussed below. Our present processing procedure gives good adhesion and an acceptable contact resistance.

### Anti-reflect Coating

The active area of the mesa-devices were coated with a single silicon nitride anti-reflect coating. The spectral reflection of a GaSb substrate control and a TPV device ITV-646-31 are shown in Fig. 12. The minimum near 1800-nm are both less than 5%. At the wavelength (1575-nm) where the absolute quantum efficiency was obtained the reflectivity is ~13%.



**Figure 12.** Reflection as a function of wavelength for a GaSb substrate and a p-on-n TPV cell (2  $\mu\text{m}$ -thick emitter-base region) having a silicon nitride anti-reflect coating.

## 5.0 TPV CELL PERFORMANCE

### 5.1 I-V Characterization

We examined the dark current-voltage characteristics of ITV646-31, which comprised a 2- $\mu\text{m}$ -thick InGaAsSb layer as shown in table I. Figure 13 shows a linear plot of dark current over the voltage interval of -2.5 to +0.45 volts. The reverse characteristic exhibits a soft breakdown beginning at about -1.5 V. The leakage at -0.5 V is 16  $\mu\text{A}$  (160  $\text{mA}/\text{cm}^2$ ), which is about double that of an InGaAs photodiode with the same cutoff wavelength.

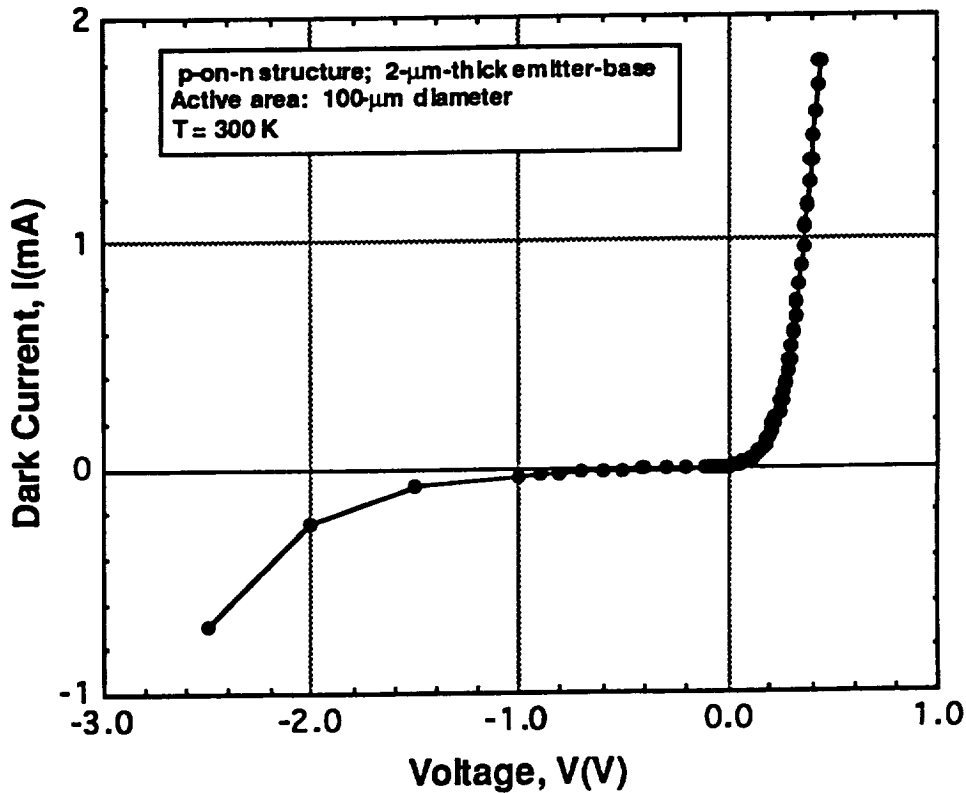


**Figure 13.** Dark I-V characteristic of ITV646-31, a p-on-n TPV structure having a 2  $\mu\text{m}$ -thick emitter-base region.

Figure 14 shows a semilogarithmic plot of the forward-biased portion of the dark current, taken from Fig. 13. Beyond a few hundredths of a volt forward bias there is not a clearly linear portion of the characteristic, and the I-V curve seems to tend toward saturation continuously. Nonetheless, as shown in Fig. 14, we assumed a linear relation in the region indicated in Fig. 14 and determined an ideality factor of 1.8. The associated saturation current was about 2.5  $\mu\text{A}$ . In the region where the current clearly tends to



saturate, we calculate a series resistance of  $40\ \Omega$ . This high value of series resistance may be due largely to our poor p-contact metallization. In addition, the large series resistance obscures the exponential dependence of the dark-current forward characteristic. At 1 mA forward current the diode is operating at a current of only  $8\ \text{A}/\text{cm}^2$ .

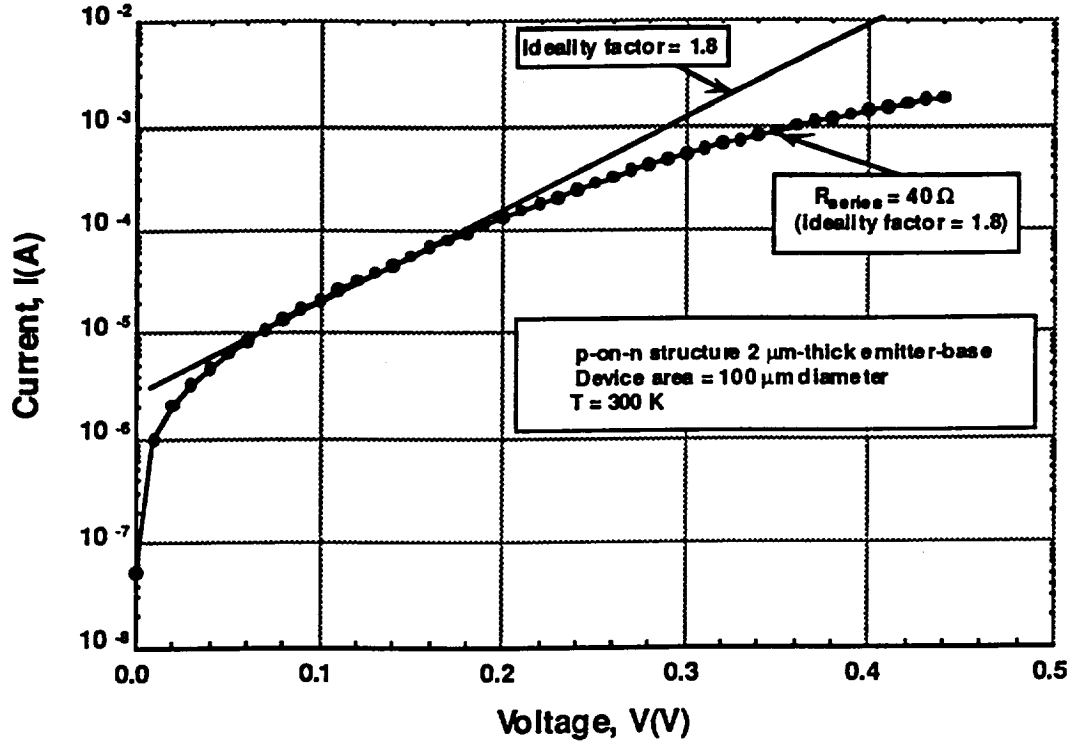


**Figure 14.** Forward dark-current characteristic for a p-on-n TPV structure having a  $2\ \mu\text{m}$ -thick emitter base region.

A thorough examination of the I-V characteristics of the TPV structures was not possible during the scope of this Phase I effort. Subsequent I-V measurements obtained in another on-going program at Sarnoff reveals more information concerning the recombination mechanisms in the InGaAsSb TPV devices and are presented below.

Figure 15. shows a semilogarithmic I-V characteristic at forward voltages less than the bandgap for a p-on-n TPV structure having a  $3.4\ \mu\text{m}$ -thick emitter-base region. The slope of this dependence gives an ideality factor of  $n > 2$ . An ideality factor of this value indicates that the current is not determined by the diffusion model at current density of practical interest but rather it is the sum of recombination through deep levels in the space charge region and tunneling. Despite this nondiffusion current contribution the absolute value of

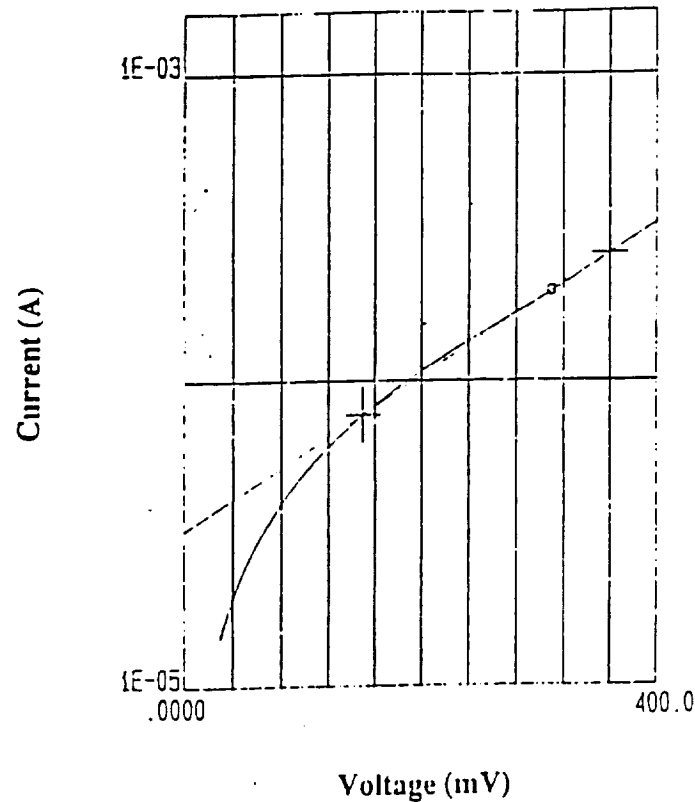


**Figure 15.** Dark I-V Characteristic for ITV-684, a p-on-n TPV structure having a 3.4  $\mu\text{m}$ -thick emitter-base region.

the forward current in the expected voltage operating range corresponds to the expected photocurrent density ( $3\text{-}10\text{ A/cm}^2$ ) in large area illuminated cells. The upper value of this expected current density ( $10\text{ A/cm}^2$ ) corresponds to a current of  $196\text{ }\mu\text{A}$  and is indicated by the lower cross-mark in Fig. 15. At this current level the applied forward voltage is  $0.31\text{ V}$ . Thus we can expect an open circuit voltage of our cells to be in the range of  $0.31\text{ V}$ .

To verify that the mechanism of the photocurrent and dark forward bias current are identical, we compared (figure 16) the dark forward bias I-V characteristic (right scale) with the induced open circuit voltage developed at different excitation levels (left scale). This measurement was obtained using a calibrated  $1.8\text{ }\mu\text{m}$  laser coupled to an optical fiber having a  $50\text{ }\mu\text{m}$  core fiber. For ease of comparison, the left scale is plotted in terms of the equivalent photo current. The equivalent photo current is equal to the numbers of photons penetrating (i.e. excluding the reflected photons) per second through the device surface.

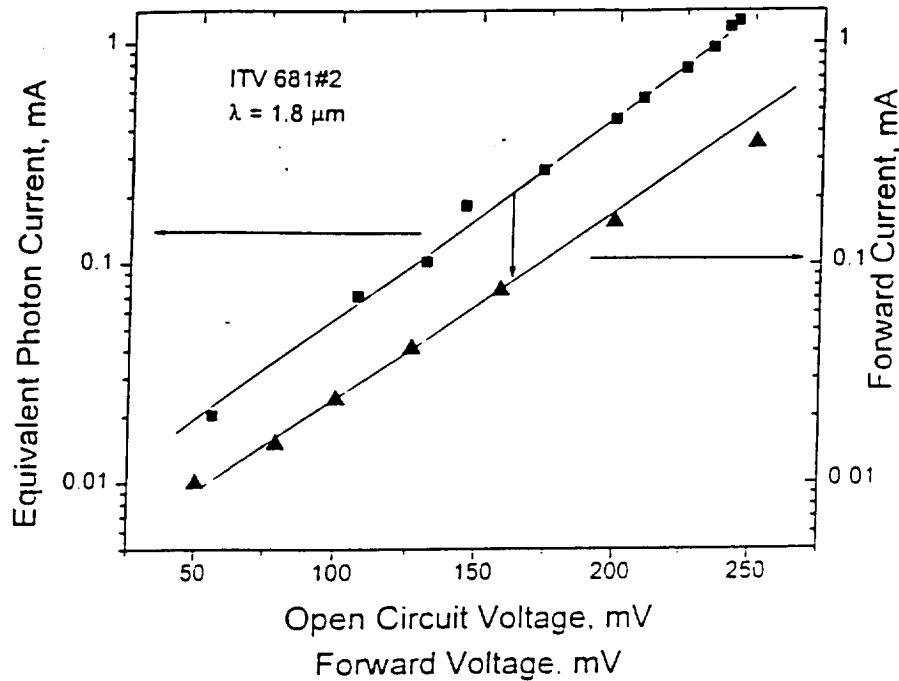


**Figure 16.** Comparison of the dark forward bias I-V characteristic (right scale) with the induced open circuit voltage developed at different excitation levels (left scale).

Since both characteristics are parallel we can conclude that the same injection recombination mechanism determines both the photocurrent and the forward bias current.

The ratio of the equivalent photocurrent to forward current at given voltage (as indicated by the arrow in figure 16) should be equal to the DQE of the samples at  $\lambda=1.8 \mu\text{m}$ . Our estimation from this dependence is 45% for this p-on-n TPV device (ITV-681) having a  $6.0 \mu\text{m}$  emitter-base region. Measurements of the spectral quantum efficiency give a value of 40% at  $1.8 \mu\text{m}$  (see Figure 25). The saturation of the forward current for currents greater than 2 mA is caused by the series resistance. As expected this saturation is not observed in the photo induced open circuit voltage since there is no current in external circuit at this high impedance voltage-current measurement.

Figure 17 shows the illuminated I-V characteristic for the TPV device shown in figure 16.

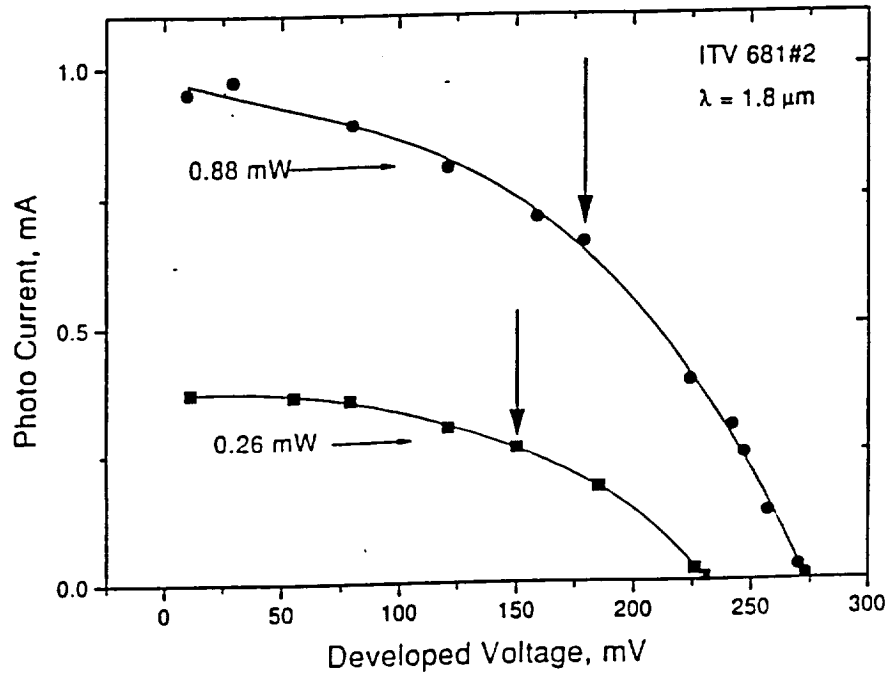
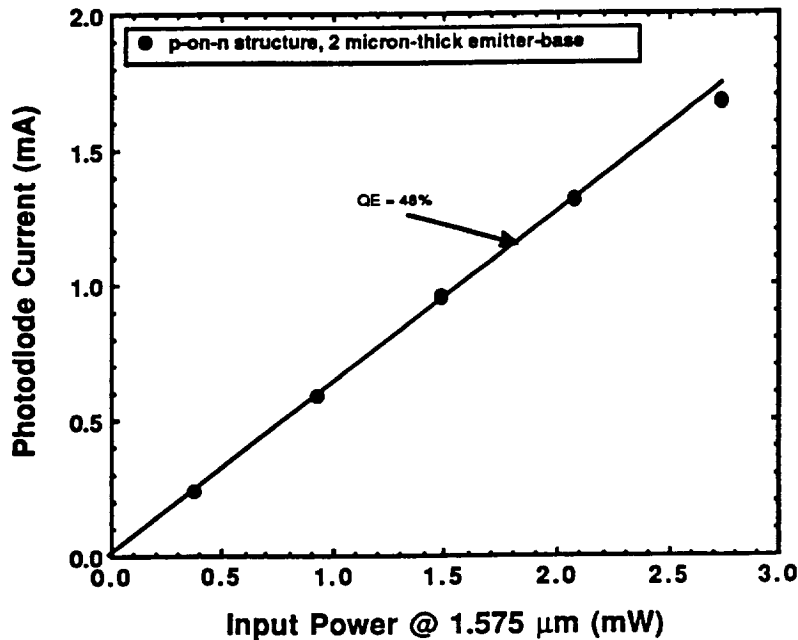


**Figure 17.** Illuminated ( $\lambda=1.8 \mu\text{m}$  emission) I-V characteristic for ITV-681, a p-on-n TPV structure having a  $6.0 \mu\text{m}$ -thick emitter-base region.

using the output of a  $1.8 \mu\text{m}$  laser. This illuminated characteristic was obtained by changing the loading from  $10 \Omega$  (corresponding to short-circuit current) to  $30 \text{ M}\Omega$  (corresponding to open circuit voltage). Two power levels of the  $1.8 \mu\text{m}$  laser are shown;  $0.26 \text{ mW}$  and  $0.88 \text{ mW}$ . At small loading values and low excitation power, the device operates as a current source with increasing voltage proportional to the increased loading. At a developed voltage greater than  $100 \text{ mV}$  the DQE cannot be considered independent of the voltage and decreases with further increasing of the loading leading to a saturation in the developed voltage. The arrows indicate the optimum loading level giving maximum power conversion for each laser power level. The fill factors for both excitation levels are about 50%.

## 5.2 External Quantum Efficiency

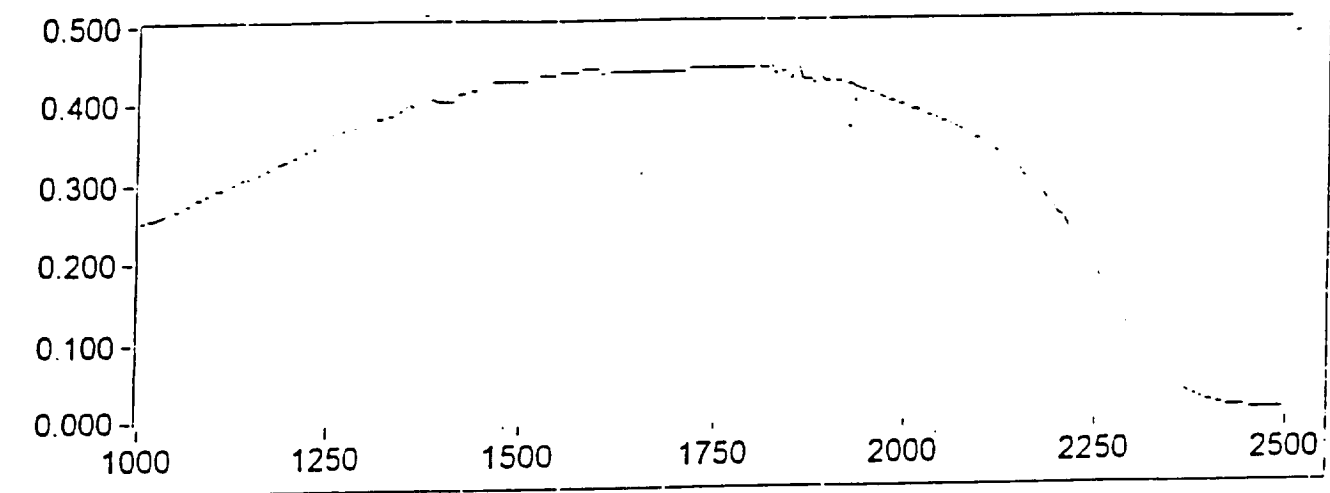
Figure 18 shows the external quantum efficiencies ( $QE_{ext}$ ) of a p-on-n structure taken at a wavelength of  $1.575\text{ }\mu\text{m}$ . The layer parameters of the structure, ITV646-31, are shown in Table 2. The efficiency was measured using a  $1.575\text{-}\mu\text{m}$  diode laser coupled to a  $9\text{-}\mu\text{m}$ -diameter fiber. The output end of the fiber was placed very close to the diode active area. The QE is linear up to an input power of  $2.1\text{ mW}$ . If we assume the power is uniform over the diode, the power density is at least  $21\text{ W/cm}^2$ . The photodiode current at this input power is  $1.3\text{ mA}$ , which is a minimum current density of  $12\text{ to }13\text{ A/cm}^2$ . At the highest input power of  $2.5\text{ mW}$ , there is a sign of photocurrent saturation, which may be the result of high series resistance. At  $1.575\text{ }\mu\text{m}$  the InGaAsSb absorption constant is about  $1\text{ }\mu\text{m}^{-1}$ , and so about  $14\%$  of the internal input radiation is absorbed in the substrate of the  $2\text{-}\mu\text{m}$ -InGaAsSb structure.



**Figure 18.** External QE at  $1.575\text{ }\mu\text{m}$  emission for p-on-n TPV structures having a  $2\text{-}\mu\text{m}$ -thick emitter-base region.

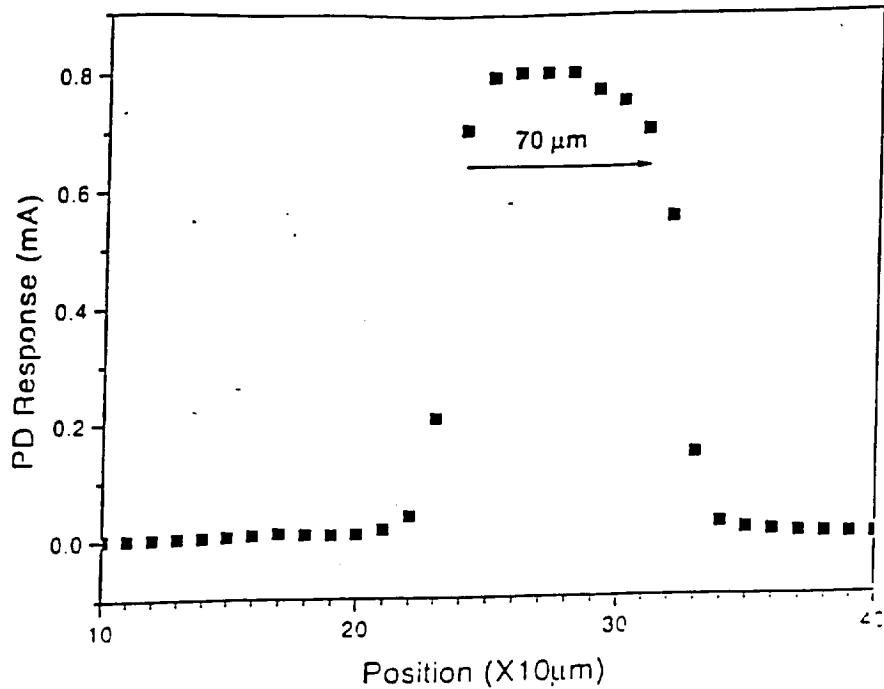
### Spectral Response

Figure 19 shows spectral photo-response for ITV646-31, structure over the wavelength interval of 1000 to 2500 nm. The added response of the GaSb substrate below 1.73  $\mu\text{m}$  is clearly seen. At longer wavelengths the response comes from the InGaAsSb, which has a long-wavelength cut-off of about 2.4  $\mu\text{m}$ .



**Figure 19.** Spectral response of ITV646-31, a p-on-n TPV structure with a 2  $\mu\text{m}$ -thick emitter-base region.

Using the fibered 1.575- $\mu\text{m}$  laser, we scanned across the diameter of diode ITV646-31, and the relative response is shown in Fig. 20. Allowing for the finite diameter of the fiber, there is no photo response outside the active area of the diode. There appears to be a nonuniformity over the surface of about 10 %, which may be the result of the many defects in this material. The conclusion is that there is no response outside the mesa, showing that the mesa was well etched into the GaSb substrate.



**Figure 20.** Relative quantum efficiency as function of position for a 100  $\mu\text{m}$  diameter etched mesa TPV device.

## 6.0 TPV MODELING

### Spectral Quantum Efficiency Measurements and Transport Parameter Extraction by Model Fitting

#### Introduction

We fit the measured spectral quantum efficiency data of ITV-646 #31 (figure #19) using a simple, one-dimensional model of photo-generated minority-carrier diffusion within the cell. During on-going research for another TPV cell development program at Sarnoff the measured SQE of two additional p-on-n TPV cells having 1- $\mu\text{m}$  bases and 3-, and 5- $\mu\text{m}$  emitters were also fit to the model. For these two structures the emitters were doped to  $10^{17} \text{ cm}^{-3}$ , and the bases were doped to  $10^{18} \text{ cm}^{-3}$ . The results obtained from the other Sarnoff program will also be included here to substantiate the TPV device parameters obtained from the model.

From the model fit the electron and hole diffusion lengths,  $L_e$  and  $L_h$ , and the interfacial recombination velocities  $s_e$  and  $s_h$ , are obtained. The most reasonable values for these parameters are  $L_e = 2 \mu\text{m}$ ,  $L_h = 1 \mu\text{m}$ ,  $S_e \approx 0 \text{ cm/s}$ , and  $S_h \approx 0 \text{ cm/s}$ . Near-zero interface recombination velocities imply perfectly reflecting barriers for minority carriers. Using these values, we calculated the optimal p-on-n and n-on-p structures, both of these device configurations had integrated quantum efficiencies (QE) of about 60 %. Their relative integrated responses to a 1000-°C blackbody were both about 50 %.

Below we discuss briefly the TPV cell configuration, the minority-carrier diffusion model and its fit to the measurements, and the optimized TPV cell structure.

### 6.1 Minority-Carrier Diffusion Model

The model assumes the exponential absorption of the input radiation transmitted into the TPV cell, the surface reflectivity,  $R$ , and the absorption constant,  $\alpha$ , each being wavelength dependent. No internal reflections are accounted for. At a given wavelength,  $\lambda$ , the minority-carrier generation rate at any point  $x$  within the TPV cell is  $F (1-R) \alpha \exp(-\alpha x) dx$  in the interval  $dx$ .  $F$  is the input photon flux at  $\lambda$ . The well-known solution to the diffusion equation is

$$n = A \sinh(x/L) + B \cosh(x/L) - K \exp(-\alpha x)$$

$A$  and  $B$  are determined by the boundary conditions, and  $K$  is a constant given by

$$K = \alpha F (1-R) \tau / (\alpha^2 L^2 - 1)$$

$\tau$  is the minority-carrier lifetime.

Figure 21 shows a schematic energy-band diagram of the p-on-n TPV cell. Also shown is



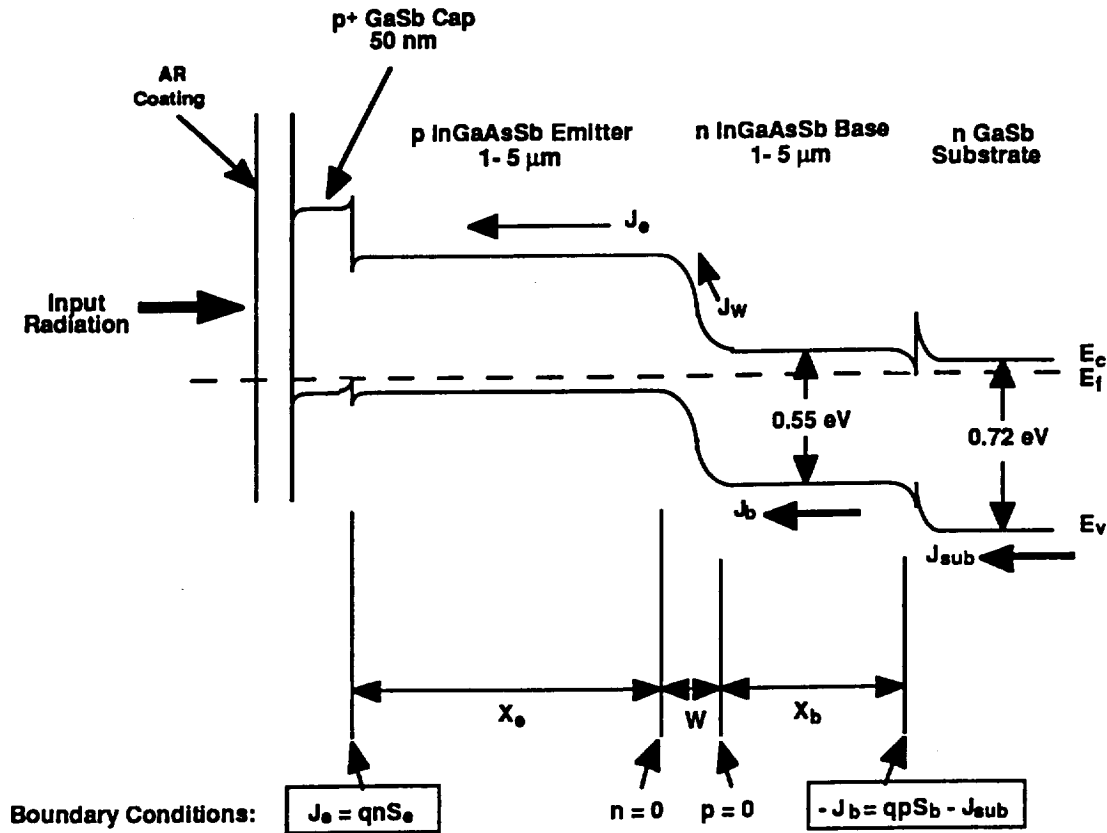


Figure 21. Schematic energy-band diagram of a p-on-n TPV cell, showing photocurrents and boundary conditions.

the notation and the four boundary conditions. The emitter thickness is  $x_e$ , the depletion width is  $W$ , and the base width is  $x_b$ . The depletion width is calculated from the standard fully-depleted junction formula, and in our case is about 0.1  $\mu\text{m}$ . Radiation enters through the emitter surface, which may be coated with an antireflection coating.

In the emitter photo-electrons diffuse towards the depletion region edge at  $x = x_e$ . The boundary condition there is that the concentration is zero, that is, all carriers reaching the junction are collected. At GaSb/InGaAsSb interface at  $x = 0$ , the minority electron current into the interface equals the concentration times the recombination velocity times, of course, the electronic charge,  $q$ . Likewise, in the base the photo-generated hole concentration is zero at the depletion region edge located at  $x = x_e + W$ . At the base/substrate interface, the minority hole current into the interface,  $-J_b(x_e + W + x_b)$ , equals the concentration of the

holes there times the interfacial recombination velocity, times  $q$ , minus any photo-generated hole current from the substrate,  $J_{sub}$ .  $J_{sub}$  arises from radiation with  $\lambda < 1.8 \mu\text{m}$  absorbed in the substrate. Such absorption occurs in TPV cells having combined emitter and base widths too narrow to absorb this short wavelength radiation fully.  $J_{sub}$  is calculated assuming a diffusion constant for holes in the GaSb substrate and assuming that the substrate extends to infinity. We observed photocurrent from the substrate in cells with  $x_e$  and  $x_b$  equal to  $1 \mu\text{m}$ .

The photocurrents from the emitter, depletion region, and base are summed to give the photocurrent total current at a given wavelength. For SQW computations  $F = 1$  at all wavelengths.  $F$  is scaled to the 1000-°C blackbody spectrum to calculate the TPV cell relative photo response to the blackbody.

## 6.2 Fit to Experimental Spectral Quantum Efficiency Measurements

All the TPV cells measured were 100- $\mu\text{m}$  diameter mesas with antireflective coatings on them. Typical coatings are shown in Figure 22.

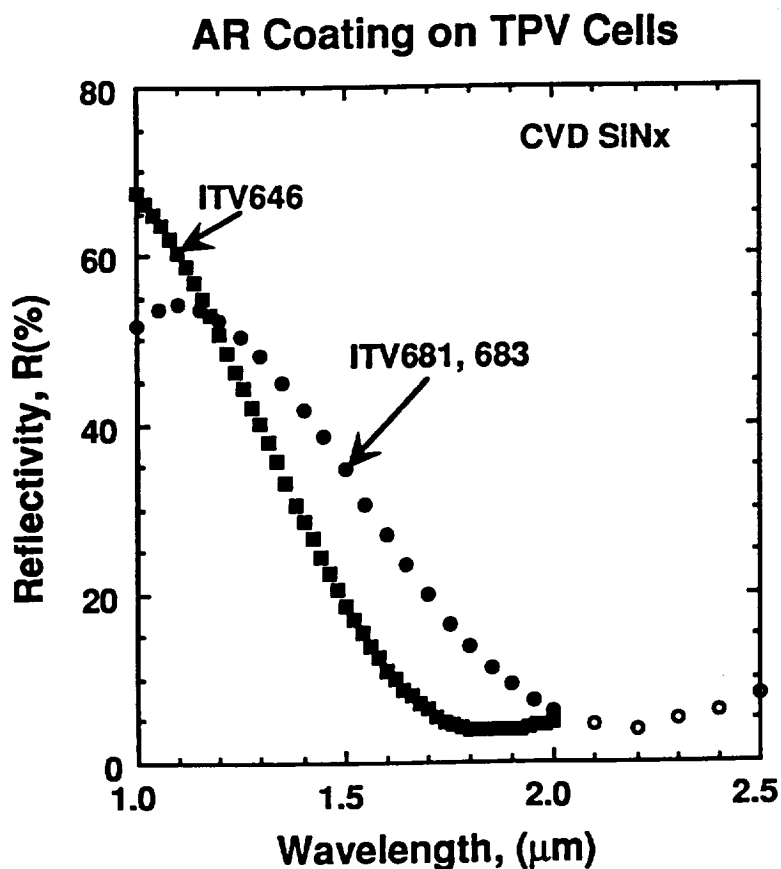


Figure 22. Antireflective coatings for the TPV cells measured.

The coating for ITV681 and ITV683 has a minimum of about 4 % at 2.2  $\mu\text{m}$  and exhibits a maximum near 1  $\mu\text{m}$ . The coating on ITV646 has a minimum at 1.8  $\mu\text{m}$  and shows no short-wavelength maximum. These reflectivity data were used in computing the model SQE curves.

Figure 23 shows the SQE for cell ITV646-31, the solid line, along with the model fit, the

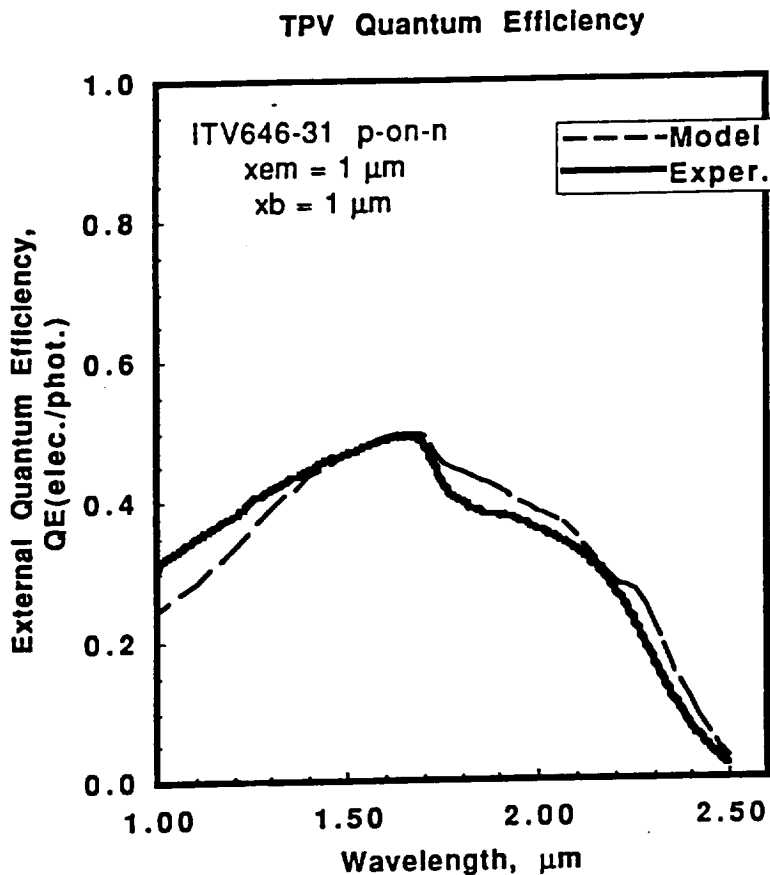


Figure 23. Spectral quantum efficiency for a p-on-n TPV cell with a 1- $\mu\text{m}$  emitter and a 1- $\mu\text{m}$  base.

dashed line. The model gives a reasonably good fit to the data. The transport parameters are  $L_e = 0.6 \mu\text{m}$ ,  $L_b = 0.7 \mu\text{m}$ ,  $S_e = 2 \times 10^5 \text{ cm/s}$ , and  $S_b = 0$ . The base and emitter dopings were reversed in this wafer, so the short electron diffusion length,  $L_e$  may be the result of too high doping, i. e.,  $10^{18} \text{ cm}^{-3}$ .

Note that we usually express recombination velocity normalized to the bulk recombination velocity,  $L/\tau$ .  $s_{ne} = S_e/(L_e/\tau_e) = 0.3$  at the emitter/cap-layer interface.  $s_{ne} \ll 1$  implies an almost perfectly reflecting interface, and  $s_{ne} \gg 1$  implies an almost perfectly minority-carrier-absorbing interface.  $s_{ne} = 1$  implies the interface absorbs particles as would occur if the interface were an extension of the bulk material. The TPV cells are designed to have zero interface recombination velocity, that is, perfectly reflecting electron and hole barriers.

The presence of a substrate photocurrent can be seen in the SQE curve as a hump in the curve at about  $1.75 \mu\text{m}$ . The model does not give as large a hump, which may be the result of the base being thinner than our assumed value of  $1 \mu\text{m}$ . At short wavelengths near  $1 \mu\text{m}$ , the model predicts a lower QE than we measure, most likely due to a difference in the antireflective coating on the cell and the one we measured, which two were assumed to be identical.

Figure 24 shows the SQE curve and the model fit for TPV cell ITV683-2, which incorporates a  $3\text{-}\mu\text{m}$  emitter and a  $1\text{-}\mu\text{m}$  base.

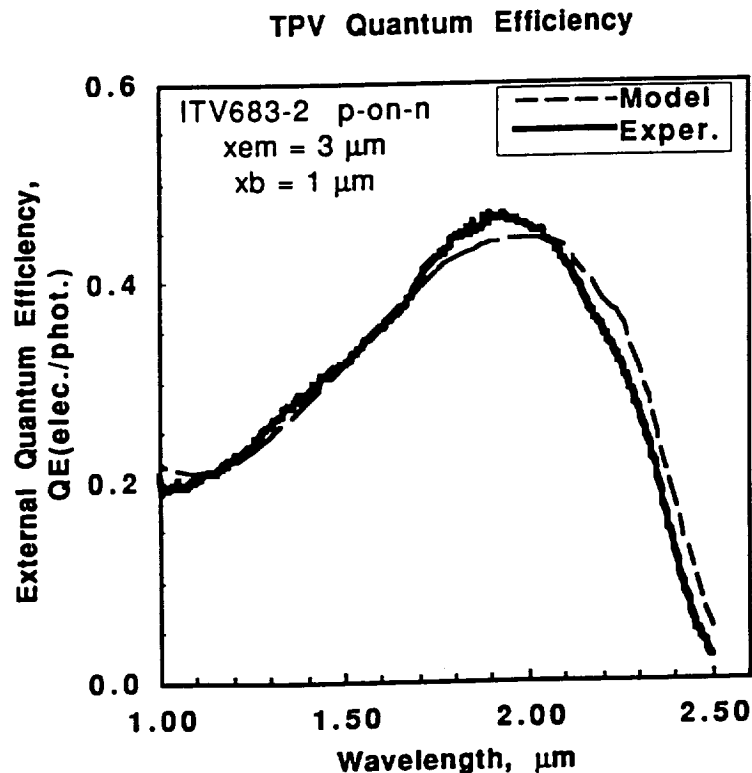


**Figure 24.** Spectral quantum efficiency and model fit to TPV cell ITV683-3, which has a  $3\text{-}\mu\text{m}$  emitter and a  $1\text{-}\mu\text{m}$  base.

The fit is good. The deviation at the long-wavelength fall-off may be due to the device having a slightly larger bandgap than the InGaAsSb we used to measure the absorption constant. The relatively low QE at shorter wavelengths is due in part to the high reflectivity of the antireflective coating. The minimum in the QE near 1- $\mu\text{m}$  predicted by the model is reflected in a lessening of the slope of the measured SQE at 1  $\mu\text{m}$ . The fit gives  $L_e = 2 \mu\text{m}$ ,  $L_b = 0.3 \mu\text{m}$ , and both  $S_e$  and  $S_b$  are zero. Note that no contribution from the substrate can be seen.

Figure 25 shows measured SQE from ITV681-3 along with the model fit. This cell had a

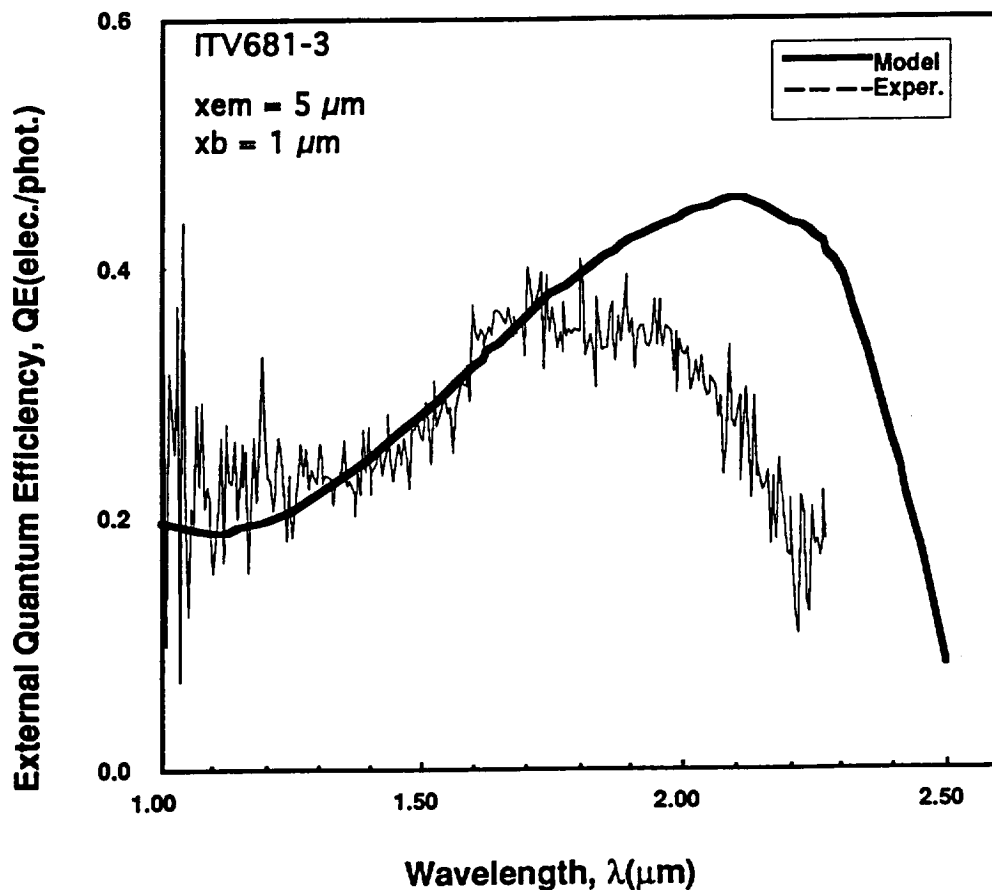


Figure 25. Spectral quantum efficiency of TPV cell ITV681-3, which has a 5- $\mu\text{m}$  emitter and a 1- $\mu\text{m}$  base.

5- $\mu\text{m}$  emitter and a 1- $\mu\text{m}$  base. The contacts on this run of devices were poor, which caused to the noisy SQE signal. With such a wide emitter the influence of the base photo response is minimal. In addition, it appears that the bandgap is much larger than the one of the InGaAsSb with which we measured the absorption constant. Attempts to use calculated absorption constants for larger bandgap InGaAsSb gave equally poor fits at the longest wavelengths. Nevertheless, at short wave lengths the effects of the antireflective coating are visible in the minimum seen in the SQE curve. The model fit gives  $L_e = 3 \mu\text{m}$ ,  $L_b = 1 \mu\text{m}$ , and again both  $S_e$  and  $S_b$  are zero.

Table III summarizes the diffusion lengths derived from the model.

**TABLE III. Model-Derived Diffusion Lengths**

$X_e(\mu\text{m})$	$L_e(\mu\text{m})$	$L_b(\mu\text{m})$
1*	0.6	0.7
3	2	0.3
5	3	1

\* emitter doping =  $10^{18} \text{ cm}^{-3}$   
 base doping =  $10^{17} \text{ cm}^{-3}$

From these data we assume that  $L_e$  is about 2  $\mu\text{m}$ , and  $L_b$  is about 1  $\mu\text{m}$ . The recombination velocities are taken to be zero. We will need more data to corroborate these estimates.

### 6.3 Optimized TPV Cell Design

Figure 26 shows the optimized p-on-n TPV cell, using  $L_e = 2 \mu\text{m}$  and  $L_b = 1 \mu\text{m}$ . The emitter is  $1.3 \mu\text{m}$  wide, and the base is  $1.7 \mu\text{m}$  wide. Also shown is the relative

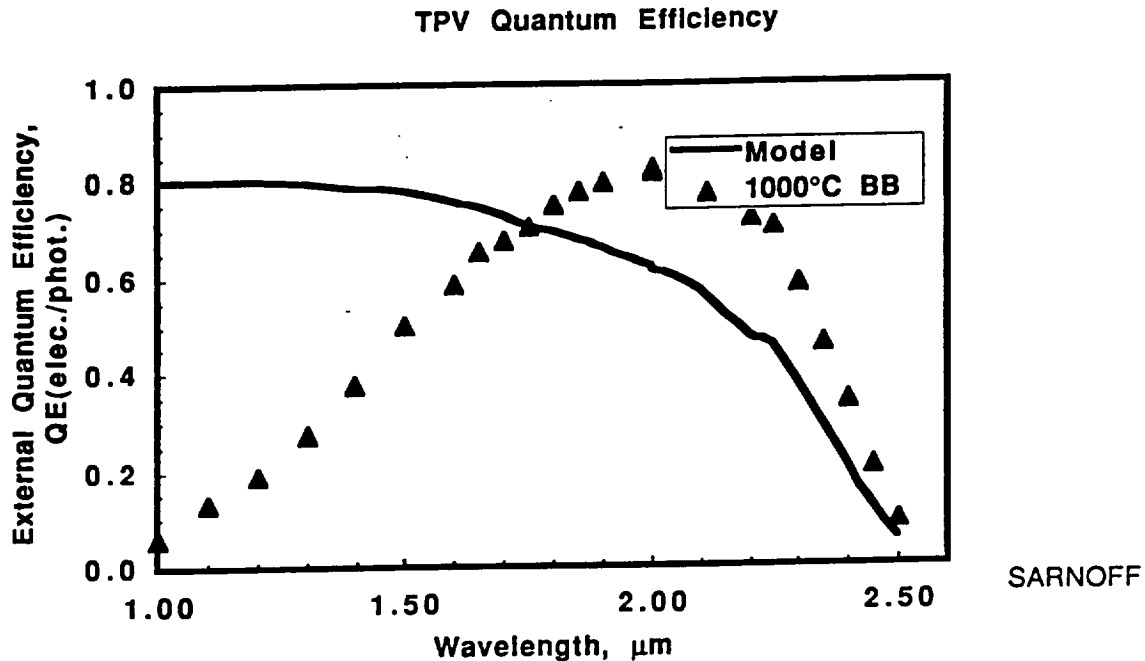


Figure 26. Optimized p-on-n TPV cell.

response to a 1000-°C blackbody emitter. It is assumed that a 5-% spectrally flat coating is applied to the cell. The integrated QE is 59 %, and the relative response to the blackbody is 50 %.

The optimized n-on-p TPV cell is shown in Fig. 27. In the n-on-p configuration, holes are the minority carriers in the emitter, and electrons are the minority carriers in the base. We, therefore, take  $L_e = 1 \mu\text{m}$ , and  $L_b = 2 \mu\text{m}$ . A 5-% antireflection coating is assumed.

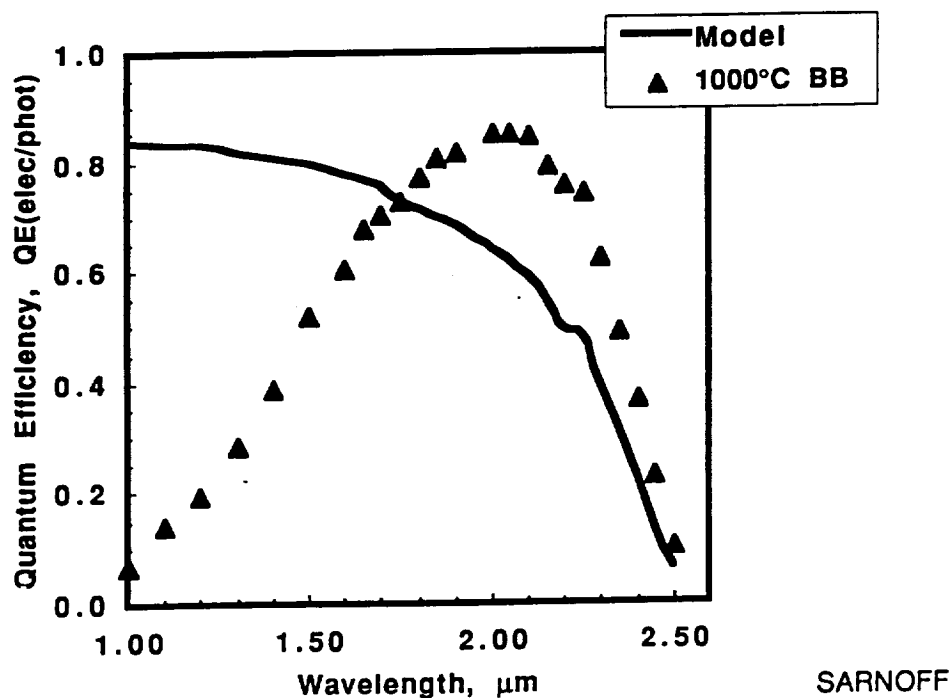


Figure 27. Optimized n-on-p TPV cell.

The recombination velocities are taken to be zero. In this case the optimal emitter is  $0.6\text{-}\mu\text{m}$  wide and the optimal base is  $2.7\text{-}\mu\text{m}$  wide. The integrated QE is 61 %, and the relative response to the blackbody is 53 %, both of these values being slightly higher than they are for the optimized p-on-n cell. Optimized p-on-n and n-on-p structures have about the same response to the blackbody, so other criteria will decide which combination to use.

It is clear from this work that to improve cell performance, the diffusion lengths of both holes and electrons must be increased. The cap/emitter and the base/substrate interfaces appear to be highly reflecting. Because the minority carrier mobilities are most likely set by alloy scattering in the InGaAsSb quaternary layers, the way to increase diffusion lengths is to improve the minority-carrier lifetimes. This, in turn, comes from improving bulk purity and quality. A benefit of such improvements is lower “saturation” currents in the forward I-V characteristic that will increase overall conversion efficiency.



## **7.0 CONCLUSION**

During this Phase I effort we have made significant progress toward the development of InGaAsSb TPV cells operating out to 2.4  $\mu\text{m}$ .

The general design issues specific to InGaAsSb TPV structures lattice-matched to GaSb substrates have been investigated. Energy-band diagrams of proposed InGaAsSb TPV structures were constructed to understand the photoexcited carrier flow in the structure and to identify aspects of the structure which might possibly limit device performance. Potential obstacles to carrier transport resulting from energy-band offsets were identified and remedies to increase transport efficiency on advanced TPV cell designs were discussed.

The material properties crucial to TPV cell performance have been determined for the InGaAsSb compounds required in these cells. A determination of these material properties is critical to the modeling and design of optimized TPV structures since very limited published material data is available for this relatively unexplored semiconductor quaternary compound.

The growth parameters for 0.55 eV InGaAsSb TPV structures lattice-matched to GaSb substrates have been determined and several p-on-n TPV structures were grown and processed into small-area (100- $\mu\text{m}$  diameter) etched-mesa devices to evaluate the performance characteristics. I-V characterization comparisons between dark and illuminated characteristics have shown that the dark forward I-V characteristic is the key for prediction of open voltage current available at a given excitation level.

An analysis of the forward I-V characteristics show that the expected value of the open circuit voltage should be in the range of 0.3 V at the expected photocurrent density of interest. For TPV cells grown for another program at Sarnoff, open circuit voltages of 0.27 V (figure 17) and 0.30 V have been obtained experimentally for laser powers of 0.88 mW and 1.2 mW (maximum available power for this laser), respectively, using a 1.8  $\mu\text{m}$  laser.

We have measured the spectral quantum efficiency of a p-on-n TPV cells having a 1- $\mu\text{m}$  emitter width and 1- $\mu\text{m}$  base width. With additional spectral quantum efficiency data for p-on-n TPV cells having a 3-, and 5- $\mu\text{m}$  emitter widths, and 1- $\mu\text{m}$  base widths, grown under another Sarnoff program, the results were fit to a model. A fit to the data gave an electron diffusion length of about 2- $\mu\text{m}$  and a hole diffusion length of about 1  $\mu\text{m}$ . The recombination velocities were nearly zero at the GaSb-cap/emitter and at the base/GaSb-substrate interfaces. Using these parameter values, we determined the structure for optimized p-on-n and n-on-p TPV cells. Each one had an integrated quantum efficiency of about 50 % and an integrated response to a 1000°C blackbody of about 60 %.

### Comparison with Published Results

Figure 28 shows a comparison of the best p-on-n result, ITV-692-2, (having a  $1.1 \times 10^{-4} \text{ cm}^2$  active area) compared with published data for n-on-p InGaAs and p-on-n InGaAsSb TPV cells having a  $1 \text{ cm}^2$  active area [6]. ITV-692 contains a 1- $\mu\text{m}$  thick emitter ( $10^{17} \text{ cm}^{-3}$ )

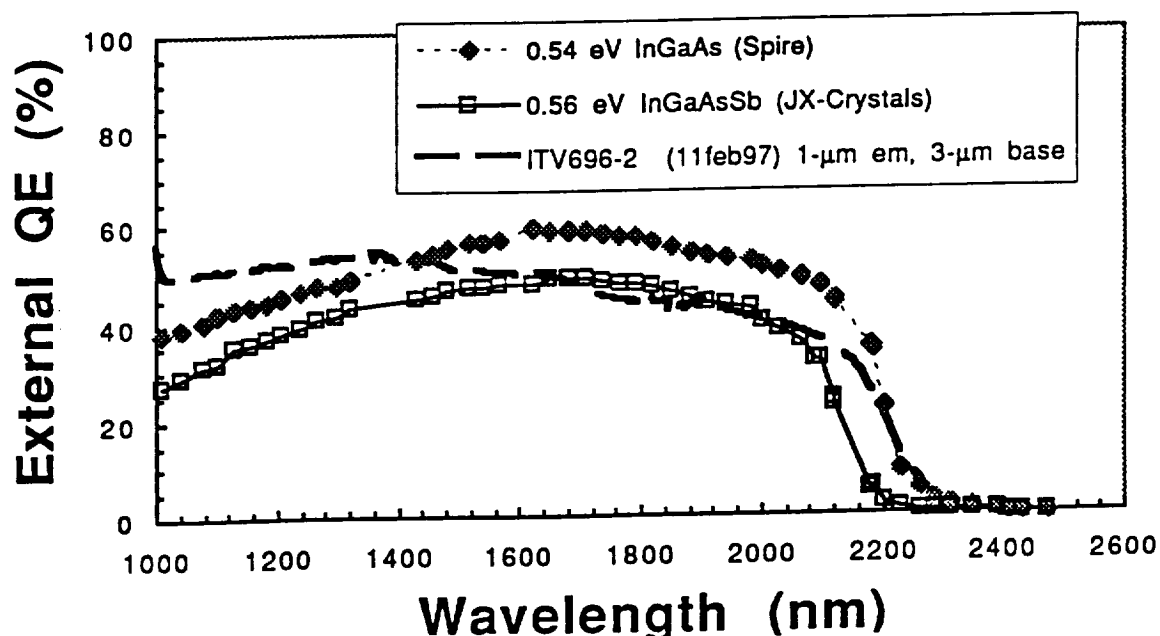


Figure 28. Comparison of a Sarnoff TPV cell with InGaAs and InGaAsSb cells.

and a 3  $\mu\text{m}$ -thick base ( $10^{18} \text{ cm}^{-3}$ ) and was developed in on-going research at Sarnoff. Both the Spire-InGaAs cell [7] and the Sarnoff-InGaAsSb cell do not contain an

antireflective coating thus the external QE would be approximately 30% higher assuming a 5% antireflection. The InGaAsSb cell does contain an antireflective coating [8].

Comparing the external quantum efficiency of the Sarnoff InGaAsSb cell with the JX-Crystal cell shows an improvement in the overall response and a significant improvement in both the short and long wavelength responses. The increased short wavelength response of the Sarnoff cell is attributed to the near-zero surface recombination at the emitter interface. More important to overall TPV current generation is the increased long wavelength response of the Sarnoff cell compared with the JX Crystal cell. The fall-off in quantum efficiency near the bandedge of the JX Crystal cell is attributed to a non-optimized base region.

Comparing the external quantum efficiency of the Sarnoff InGaAsSb cell with the Spire InGaAs cell shows a superior short wavelength response for the Sarnoff cell (again attributed to near-zero surface recombination) but superior long wavelength response for the Spire cell. As discussed above, increased quantum efficiency of the Sarnoff InGaAsSb cell will be achieved for cells having increased the minority-carrier lifetimes. This comes from improving bulk purity and quality. A benefit of such improvements is lower "saturation" currents in the forward I-V characteristic that will increase overall conversion efficiency.

Methods to improve the overall performance of the InGaAsSb TPV cells through increased minority-carrier lifetimes and other improvements to the structure will be discussed in further detail in the Phase II proposal. The advantages of the lattice-matched InGaAsSb TPV cell compared to the strained InGaAs TPV cell include a simpler device structure and tunneling reverse-bias breakdown which eliminates the need of bypass diodes in high voltage arrays [6].

To summarize, the major achievements completed in this phase I effort are:

- Critical design issues relating to carrier transport investigated.
- InGaAsSb characteristics important to TPV cell design determined.
- Growth parameters and fabrication processes for InGaAsSb TPV cells determined.
- Prototype InGaAsSb TPV cells grown and evaluated.
- Computer modeling program developed to predict spectral quantum efficiency.
- Carrier diffusion lengths and surface/interfacial recombination velocities determined.
- Dark-forward I-V characteristic identified as key to predict open circuit voltage.
- Superior spectral quantum efficiency for InGaAsSb TPV cells achieved.
- Optimized TPV structure design obtained by computer model.

## 8.0 REFERENCES

1. Y. Tsou, A. Ichii, and Elsa M. Garmire, "Improving InAs Double Heterostructure Lasers with Better Confinement," *J. Quantum Electron.*, **28**, 1261, 1992.
2. H. Lee, P. K. York, R. J. Menna, R. U. Martinelli, D. Z. Garbuzov and S. Y. Narayan, "2.78- $\mu\text{m}$  InGaAsSb/AlGaAsSb Multiple Quantum-Well Lasers with Metastable InGaAsSb wells grown by molecular Beam Epitaxy" *Journal of Crystal Growth*, **150**, 1995.
3. R. U. Martinelli and G. H. Olsen, "Improved Transmission Secondary Emission from  $\text{In}_x\text{Ga}_{1-x}\text{P}$ /GaAs Self-Supporting Films Activated to Negative Electron Affinity", *J. Appl. Phys.*, **47**, 1332-1336, 1976
4. G. W. Turner, S. J. Eglash, and A. J. Strauss, "Molecular-Beam Epitaxial Growth of High-Mobility n-GaSb," *J. Vac. Sci. Technol.*, **B11**, 1993.
5. G. W. Turner, S. J. Eglash, and A. J. Strauss, "Molecular-Beam Epitaxial Growth of High-Mobility n-GaSb," *J. Vac. Sci. Technol.*, **B11**, 1993.
6. G. W. Charache, J. L. Egley, L. R. Danielson, D. M. DePoy, P. F. Baldasaro, B. C. Campbell, S. Hui, L. M. Fraas, and S. J. Wojtczuk, "Current Status of Low-Temperature Radiator Thermophotovoltaic Devices, Presented at 25th IEEE Photovoltaics Specialist Conference, 1996.
7. S. Wojtczuk, P. Colter, G. Charache, and B. Campbell, "Production Data on 0.55 eV InGaAs Thermophotovoltaic Cells," Presented at 25th IEEE Photovoltaics Specialist Conference, 1996.
8. G. Charache, private communication.



REPORT DOCUMENTATION PAGE			Form Approved OMB No. 0704-0188	
Public reporting burden for this collection of information is estimated to average 1 hour per response, including the time for reviewing instructions, searching existing data sources, gathering and maintaining the data needed, and completing and reviewing the collection of information. Send comments regarding this burden estimate or any other aspect of this collection of information, including suggestions for reducing this burden, to Washington Headquarters Services, Directorate for Information Operations and Reports, 1215 Jefferson Davis Highway, Suite 1204, Arlington, VA 22202-4302, and to the Office of Management and Budget, Paperwork Reduction Project (0704-0188), Washington, DC 20503.				
1. AGENCY USE ONLY (Leave blank)		2. REPORT DATE September 1997		3. REPORT TYPE AND DATES COVERED Final Contractor Report
4. TITLE AND SUBTITLE InGaAsSb/GaSb Thermophotovoltaic Cells Phase I Effort			5. FUNDING NUMBERS  WU-241-02-0J C-NAS3-96060	
6. AUTHOR(S)  Yabo Li, Gary S. Tompa, Nancy Morris, John Connolly, and Hao Lee				
7. PERFORMING ORGANIZATION NAME(S) AND ADDRESS(ES)  Structured Materials Industries, Inc. 120 Centennial Avenue Piscataway, New Jersey 08854-3908			8. PERFORMING ORGANIZATION REPORT NUMBER  E-10902 SMI41132-Final	
9. SPONSORING/MONITORING AGENCY NAME(S) AND ADDRESS(ES)  National Aeronautics and Space Administration Lewis Research Center Cleveland, Ohio 44135-3191			10. SPONSORING/MONITORING AGENCY REPORT NUMBER  NASA CR-204146	
11. SUPPLEMENTARY NOTES  Work funded by BMDO Small Business Innovation Research Contract NAS3-96060. Project Manager, David Wilt, Power Technology Division, NASA Lewis Research Center, organization code 5410, (216) 433-6293.				
12a. DISTRIBUTION/AVAILABILITY STATEMENT  Unclassified - Unlimited Released as Publicly Available August 1997 Subject Category 44  This publication is available from the NASA Center for AeroSpace Information, (301) 621-0390.			12b. DISTRIBUTION CODE	
13. ABSTRACT (Maximum 200 words)  The goal of this Phase I effort was to demonstrate the growth and fabrication techniques for an InGaAsSb-based thermophotovoltaic (TPV) cell operating out to 2.5 $\mu\text{m}$ that would enable efficient electrical power production from either exothermic reactions (fuel combustion) or radioisotope thermal sources. The TPV cells were grown by molecular beam epitaxy (MBE) and consisted of an InGaAsSb double-heterostructure fabricated on a GaSb substrate. The InGaAsSb composition was lattice matched to the GaSb substrate to eliminate dislocation densities at the growth interface, a common problem with InGaAs-based TPV cell technologies. A p-on-n configuration was used to reduce overall free carrier absorption for the incorporation of a back surface reflector.				
14. SUBJECT TERMS  Thermophotovoltaics, Indium gallium antimonide arsenides			15. NUMBER OF PAGES 43	
			16. PRICE CODE A04	
17. SECURITY CLASSIFICATION OF REPORT Unclassified	18. SECURITY CLASSIFICATION OF THIS PAGE Unclassified	19. SECURITY CLASSIFICATION OF ABSTRACT Unclassified	20. LIMITATION OF ABSTRACT	